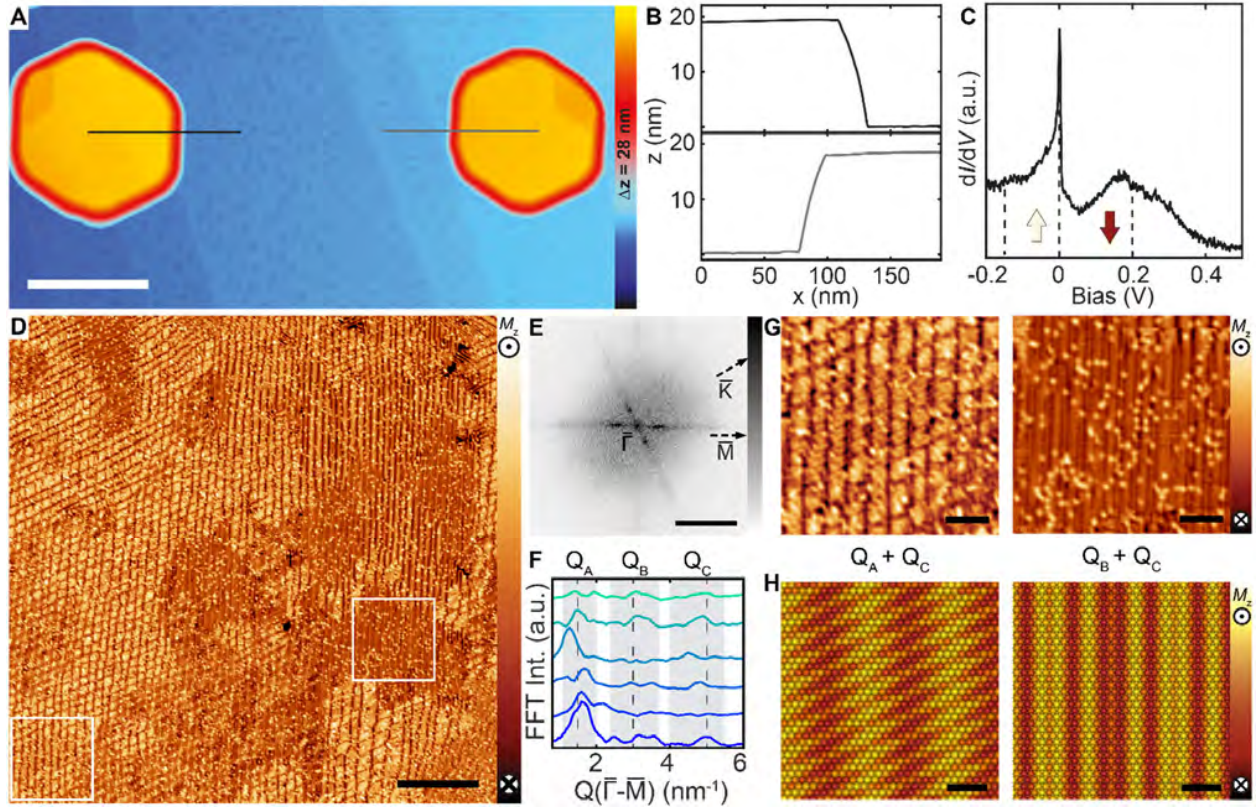**Figure captions**

Fig 1: Imaging the spin Q-glass state of Nd(0001): (**A**) Constant-current STM image of a Stranski-Krastanov grown Nd film on W(110), revealing nearly flat-top islands on a Nd wetting layer. The surface defect concentration is less than 0.01 ML (scale bar = 150 nm, V_S = 1 V, I_t = 20 pA). (**B**) Line profiles along the indicated island edges. The thickness of each island is larger than 50 ML. (**C**) dI/dV spectrum acquired on the Nd(0001) surface, showing the exchange-split surface state (V_{stab} = 1 V, I_{stab} = 200 pA, V_{mod} = 1 mV; T = 40 mK). (**D**) Magnetization image illustrating the spatially complex magnetic ground state of a spin-Q glass, which lacks long-range order (T = 1.3 K, B = 0 T, I_t = 200 pA). The contrast is directly related to variations in the out-of-plane magnetization (M_z) imaged with an out-of-plane sensitive Cr bulk tip (scale bar = 50 nm). (**E**) Q-space image of the magnetization image in (D) (scale bar = 5 nm^{-1}), illustrating a large distribution of states in Q space. (**F**) Line-cuts along $\bar{\Gamma}$-$\bar{M}$ of various Q-space images taken from smaller sections of the image in (D) (cf. Fig. S5). (**G**) Close-up views of regions marked in (D), illustrating the local spatial variation of the magnetic order (scale bar = 10 nm). (**H**) Schematic of the out-of-plane projected magnetization resulting from a superposition of the labelled Q vectors (scale bar = 2 nm). The wave vector amplitudes used are marked with dashed lines in (F).
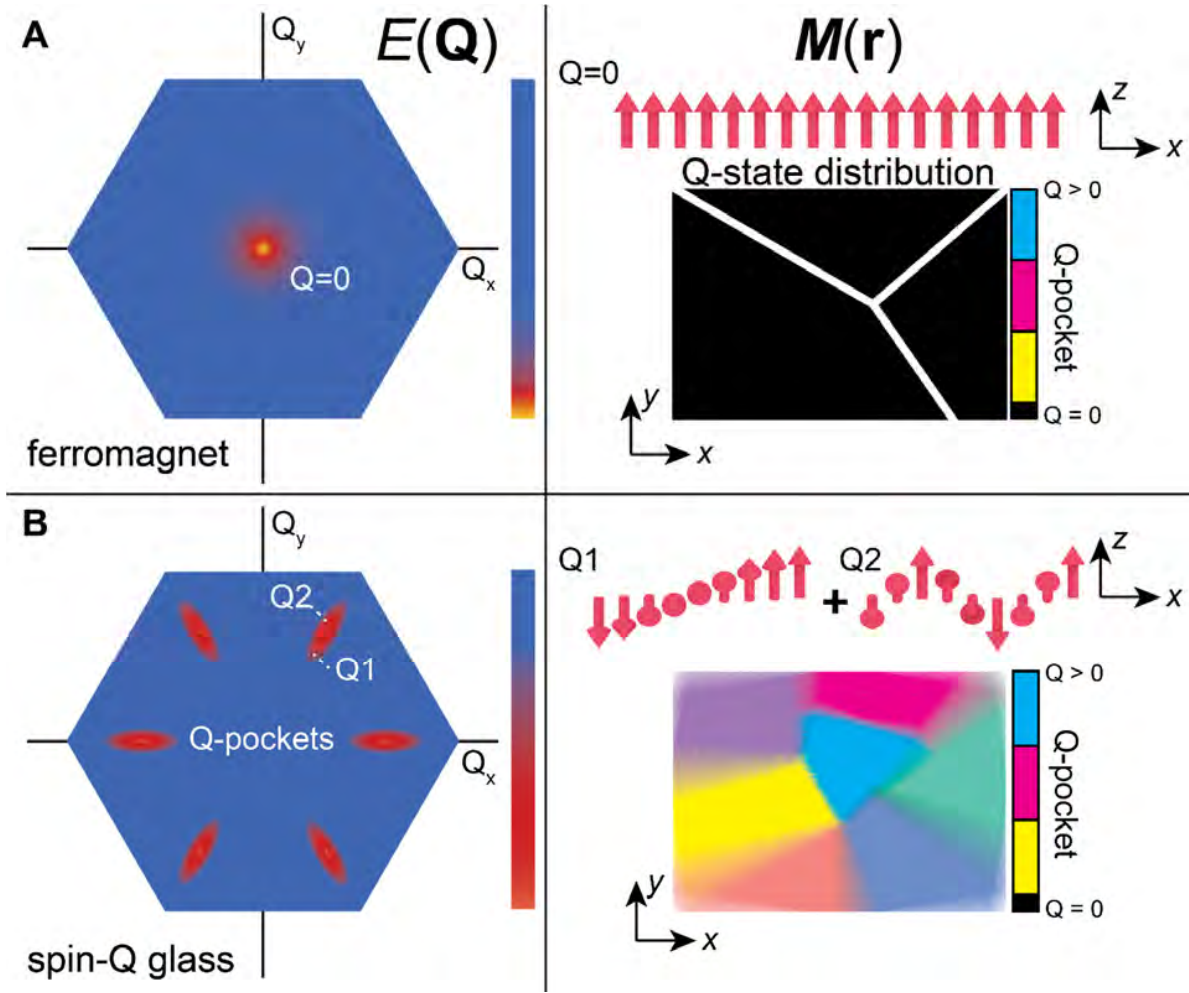
Fig 2: Energy landscape of a spin-Q glass: (**A**) Q-space image of the energy landscape $E(\mathbf{Q})$ of a prototypical ferromagnet, which exhibits a strong global minimum at Q = 0, corresponding to a real-space magnetization pattern $M(\mathbf{r})$ where all spins are aligned. Further minimization leads to the formation of distinct domains (black), separated by domain walls (white), but all domains are defined by a repeating Q-state distribution, where Q = 0. (**B**) A characteristic Q-space image for a spin-Q glass, which can be distinguished by flat valleys (Q-pockets) at non-zero Q values, which leads to a superposition of a distribution of Q states with different periodicities residing in each pocket. This results in a complex $M(\mathbf{r})$ pattern that lacks long-range order. The spatial distribution of Q states contains regions with local order defined by mixing of Q states (colors) derived from the given Q pockets.
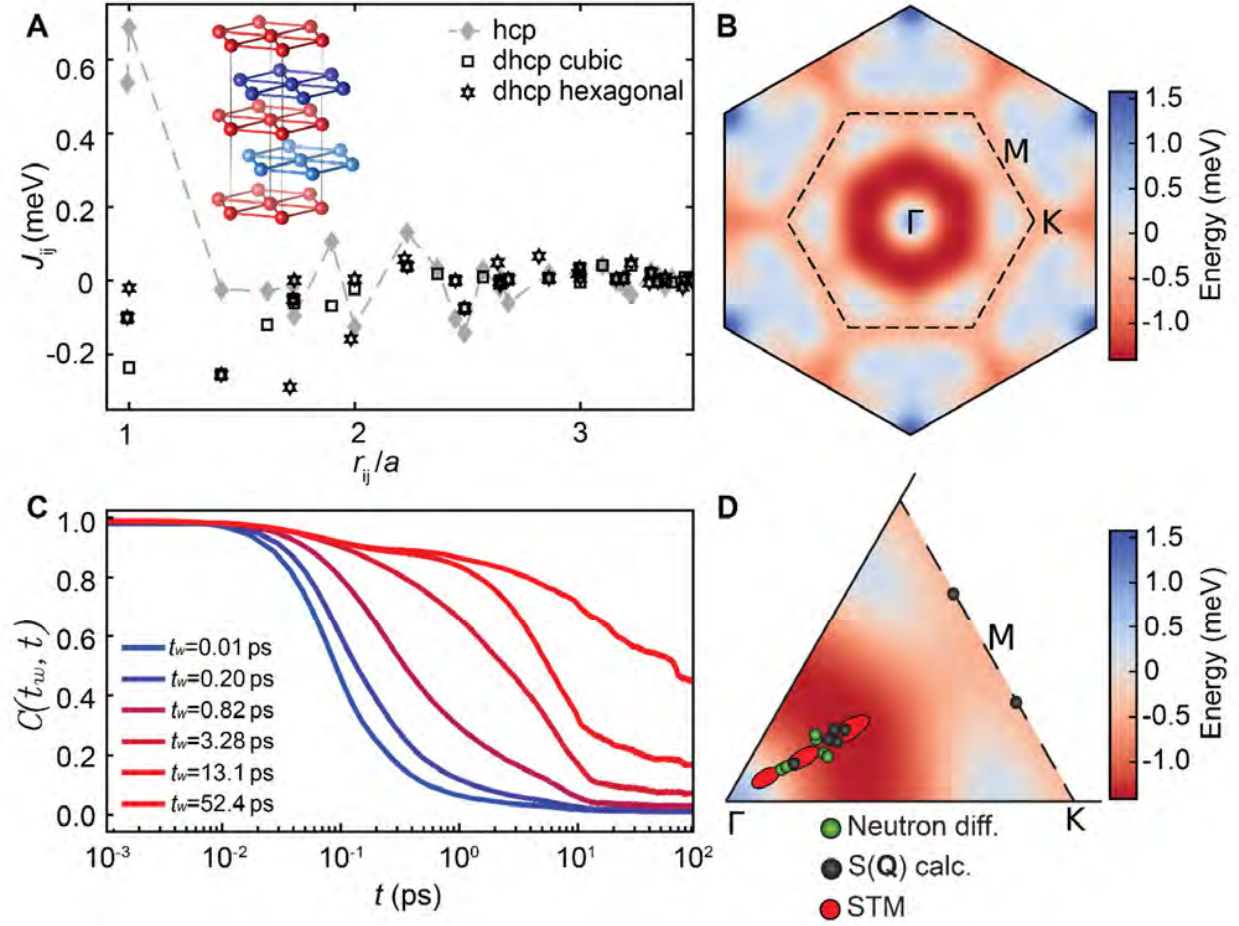
Fig 3: Elemental Nd electronic and magnetic landscape: (**A**) Calculated Heisenberg magnetic exchange interactions among Nd spin moments with magnitude 2.454 μ_B, both in the dhcp Nd (black) and the hypothetical hcp structure (gray). A negative interaction denotes a preference for an antiferromagnetic alignment among the spins, while a positive one denotes a ferromagnetic alignment. Inset: the dhcp crystal structure, with an ABAC stacking, where the cubic A sites are represented by red spheres, and the hexagonal B and C sites by light and dark blue spheres, respectively. (**B**) Energy landscape for single-Q spin spirals with $Q = (Q_x, Q_y, 2\pi/c)$ as evaluated from the calculated exchange interactions for the dhcp structure. (**C**) Autocorrelation function $C(t_w, t) = \langle \boldsymbol{m}_i(t + t_w) \cdot \boldsymbol{m}_i(t_w) \rangle$ for dhcp Nd at $T = 1$ K. (**D**) Comparison of Q states for: SP-STM (this work, red), neutron diffraction (Ref. (*21, 25*), green) and simulations (this work, black).
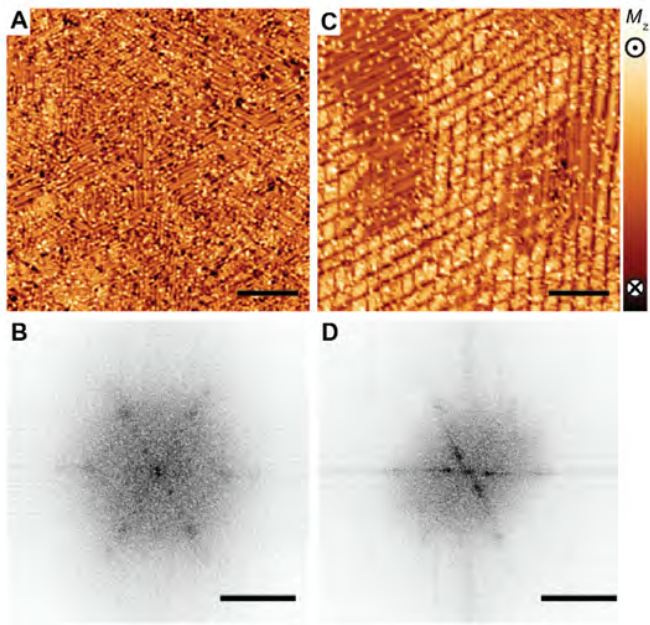
Fig 4: Effect of defects on the spin-Q glass state: Magnetization and the corresponding Q-space images of (**A**, **B**) a dirty surface (surface defect concentration of 0.03 ML) and (**C**, **D**) a clean surface (<0.01 ML) (scale bar = 20 nm, I_t = 200 pA for magnetization images, and scale bar = 5 nm^{-1} for Q-space images, inverted grey scale). Higher amount of contamination results in pinning of the Q-state around the defects, as illustrated in real space magnetization images. Overall, measurements of several samples showed that the Q-state distribution is essentially unaltered for concentrations ≤ 0.014 ML. The Q-space image of the dirty sample shows more well-defined Q-pockets as a consequence of the pinning, in contrast to the smeared out Q-pockets along the high symmetry axes in the clean sample.
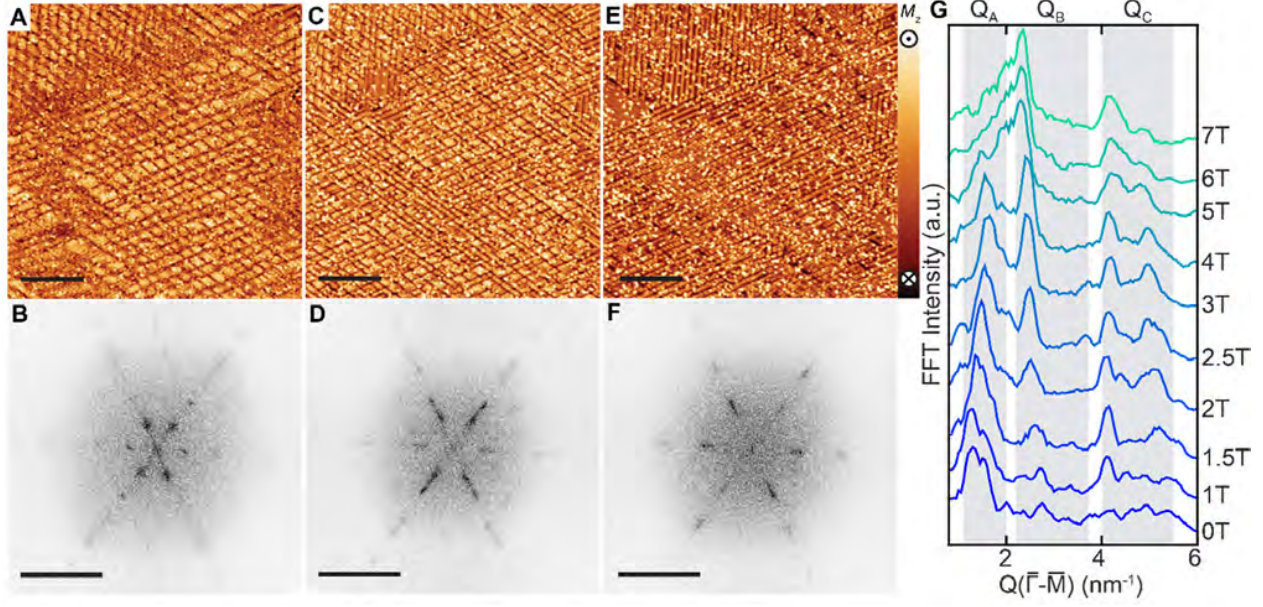
Fig 5: Magnetic field evolution of the spin-Q glass state: Magnetization and the corresponding Q-space images of the same area measured at T = 1.3 K, (**A**, **B**) in B_z = 0 T, (**C**, **D**) in B_z = 4 T, and (**E**, **F**) in B_z = 7 T (scale bar = 30 nm, I_t = 200 pA for magnetization images, and scale bar = 4 nm^{-1} for Q-space images, inverted grey scale). Increasing magnetic field does not favor a low Q state, nor exhibits the favorability of any Q state, illuminated by the broadening of the spectral weight in the various pockets. (**G**) Line-cuts along $\bar{\Gamma}$-$\bar{M}$ of Q-space images (Fig. S11) with finer intervals of increasing B_z. The spectral distribution becomes smeared out within the given pockets leading to no well-defined long-range periodicity at the highest B_z. The surface defect concentration is 0.01 ML.
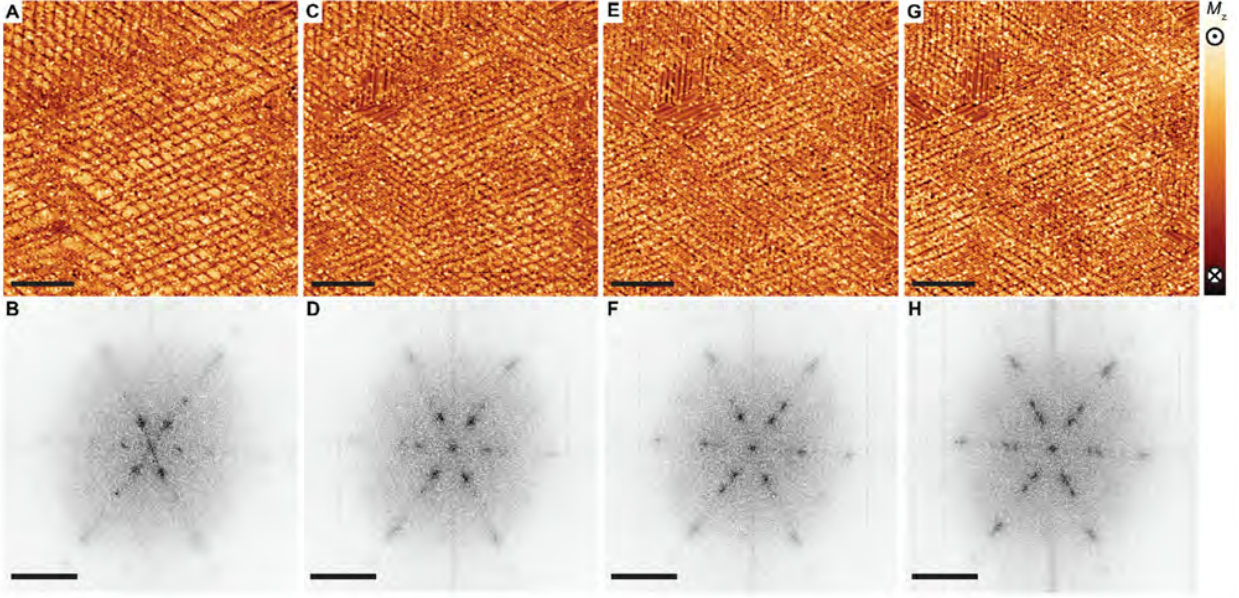
Fig 6: Aging and glassy behavior of the spin-Q glass state: (**A**, **B**) Magnetization and the corresponding Q-space images of the surface at T = 1.3 K, in its pristine state at B = 0 T. The same measurements were performed at the exact same area in B = 0 T after subsequent magnetic field sweeps and intermittent probing, leading to the magnetization and Q-space images (**C**, **D**) after $B_{z,1}$ = +4 T, τ_1 = 10^5 s, (**E**, **F**) after $B_{z,2}$ = -4 T, τ_2 = 10^5 s and (**G**, **H**) after $B_{z,3}$ = +7 T, τ_3 = 10^5 s. Typical sweep rates were on the order of 225 mT/min. The sequence shows that the system never reverts to the initial zero-field-cooled state (scale bar = 30 nm, I_t = 200 pA for magnetization images, and scale bar = 4 nm^{-1} for Q-space images, inverted grey scale). The surface defect concentration is 0.01 ML.
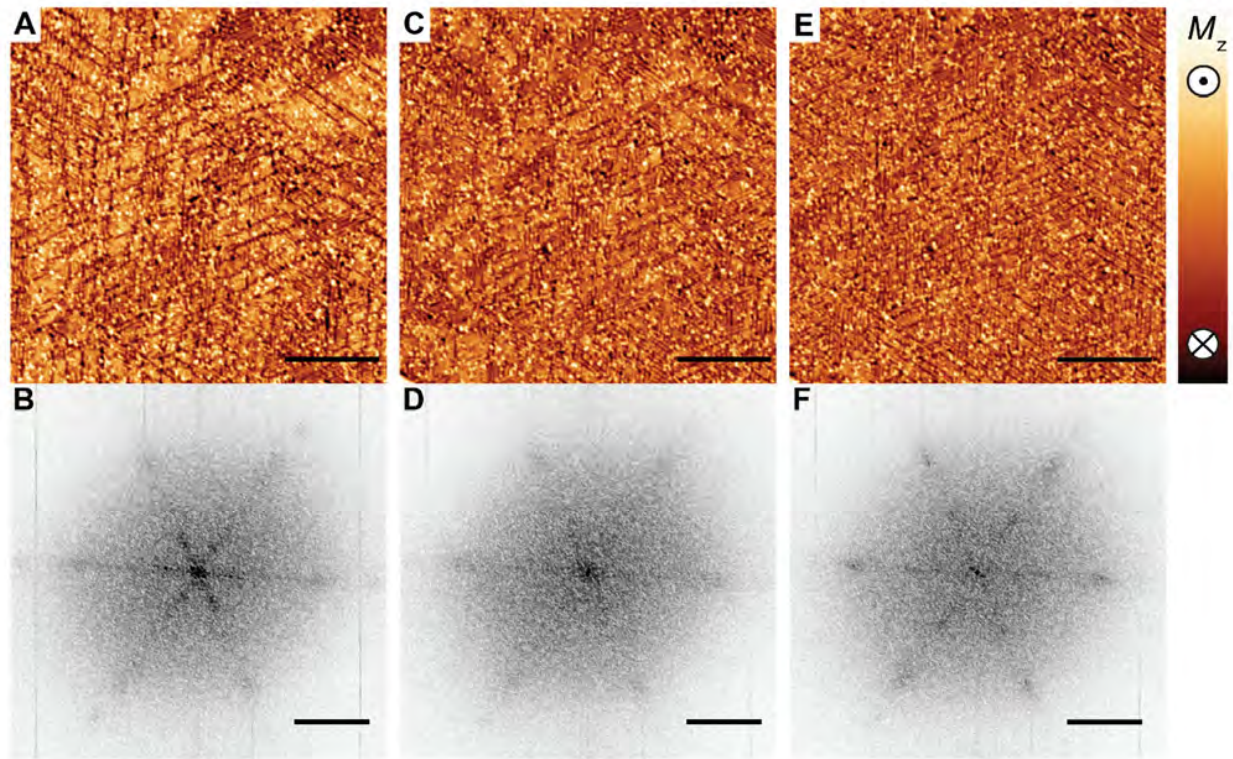
Fig 7: Temperature dependence of the spin-Q glass state: Magnetization and the corresponding Q-space images of the exact same are (**A**, **B**) at $T = 1.3$ K and (**C**, **D**) at $T = 4.2$ K, in $B = 0$ T. Warming up the surface from 1.3 K to 4.2 K results in depopulation of the Q_A pocket. (**E**, **F**) The same measurements were performed after +4T magnetic field sweep in the same area at $T = 4.2$ K in $B = 0$ T, illustrating similar out-of-plane magnetic field aging behavior (scale bar = 30 nm, $I_t = 200$ pA for magnetization images, and scale bar = 3 nm^{-1} for Q-space images, inverted grey scale). The surface defect concentration is 0.01 ML.

Supplementary Materials

Self-induced spin glass state in elemental and crystalline neodymium

Umut Kamber, Anders Bergman, Andreas Eich, Diana Iuşan, Manuel Steinbrecher, Nadine Hauptmann, Lars Nordström, Mikhail I. Katsnelson, Daniel Wegner, Olle Eriksson, Alexander A. Khajetoorians

correspondence to: a.khajetoorians@science.ru.nl, d.wegner@science.ru.nl

Contents

S1 - Growth and morphology of Nd(0001) SK islands and closed films

The motivation for growing films of Nd rather than using bulk single crystals comes from the well-known difficulty of cleaning the surface of bulk crystals of the lanthanide metals, due to severe segregation of bulk impurities toward the surface (*30, 37, 73*). Only after extremely long sputter-anneal cycles, few groups reported successful reduction of bulk impurity segregation such that the surface state could be observed, although surface contamination was still detectable via Auger electron spectroscopy (AES). The alternative approach of epitaxially growing lanthanide films on various 4*d* and 5*d* single crystal substrates (mostly bcc(110) surfaces of W, Mo and Nb were used) has been studied extensively in literature, resulting in high-quality crystals (mosaicities <0.1º) with a (0001) surface orientation and with impurity concentrations below the AES or ARPES detection limit (*29, 31, 35, 36, 39, 41, 44, 45, 48, 74-78*). It was confirmed that various lanthanide (including Nd) thin films of >10 monolayers (ML) are strain-free and possess bulk lattice constants; the electronic structure is fully developed at 30 ML, and long-range magnetic order is bulk-like in the range of 30-50 ML (*27, 29, 31-33, 35, 36, 38-49, 51, 74-93*). For Nd, the dhcp structure with bulk lattice constants was confirmed, independent of the substrate used (*34, 35, 38, 46, 77*). Moreover, neutron and XRD scattering studies on films and superlattices found magnetic peaks identical to those of bulk samples for thin Nd films down to 33-39 ML (*38, 46, 47*). We note that in one study of Nd/Sm superlattices additional magnetic satellite peaks have been observed that are not known from any Nd bulk studies (*77*), however, as Sm also orders magnetically, this can be ascribed to some interlayer coupling effects of the superlattice. In summary, epitaxial lanthanide films of sufficient thickness provide superior bulk and surface cleanliness while fully maintaining all bulk properties.

Measurements were performed on epitaxial islands of Nd(0001) grown on W(110). The W(110) substrate was cleaned by repeated cycles of annealing at T = 1250°C in a gradually reduced oxygen atmosphere (from p = 1 x 10^{-7} mbar in the first cycle down to p = 2 x 10^{-8}) and flashing at T = 2400°C, as described in Ref. (*94*). W(110) surfaces that showed insignificant contamination of oxygen or carbon were used for subsequent Nd growth, as done previously in temperature-dependent experiments (*27, 54*). The Nd source material was purchased from AMES laboratory (www.ameslab.org; purity 4N, see Table S1 for the most abundant elemental impurity concentrations), which was melted and then thoroughly degassed under UHV conditions inside the crucible of an electron-beam evaporator, in order to further reduce the contamination from oxygen and hydrogen. For the growth of Nd films, the material was sublimated from the electron-beam evaporator and deposited onto the W(110) kept at room temperature. Subsequent annealing at T = 700°C for 15 minutes resulted in either a Stranski-Krastanov (SK) growth when the nominal film thickness was smaller, or an ordered closed film with an atomically smooth surface (*48*). Fig. S1A illustrates a typical large-scale STM image after growth of ca. 15 ML Nd and subsequent annealing. Large islands of Nd, on the order of hundreds of nanometers in diameter and > 50 ML high were typically observed (cf. line profile in Fig. 1B). The surface was relatively flat with atomic steps visible from either locally varying thickness or overgrown steps at the interface to the W substrate (Fig. S1B). Such islands

showed the expected exchange-split surface state of Nd(0001) (Fig. 1C) (*27, 54*). Fig. S1C shows the topography of a ~100 ML thick Nd film after the same annealing procedure. The larger nominal coverage would have required a much higher annealing temperature to lead to SK growth (*48*). In this case, the annealing temperature was sufficient to create a well-ordered and atomically smooth surface, but the layers did not yet break up to form the thermodynamically more stable SK islands. A major difference in the morphology of the two samples was the presence of dislocations. Despite an overall high crystallinity, extended dislocations could be identified in the image area of the closed thick film (*51, 80*), while all sufficiently annealed SK islands were free of dislocations.

At this point, we would like to comment on the morphology of the sample. AC-susceptibility (*42, 48*), SP-STM (*49, 82, 94*) and STS (*27, 49, 54, 79, 92*) studies on various lanthanide metals showed that SK-grown islands reflect bulk magnetic properties, provided they are sufficiently thick. The advantage of SK-grown islands is that strain relief is better than in layer-by-layer grown films, that is misfit dislocations (due to lattice mismatch at the interface) and screw dislocations (caused by antiphase boundaries created in the initial growth) can be avoided (*39, 40, 49, 91*). To check whether there might be any finite-size effect present in our samples, we investigated different islands with various volumes that is with heights ranging from 58 to 92 ML and with lateral areas ranging from 58000 to 200000 nm^2. All results reported here were consistently observed on all these differently sized islands. Moreover, we also studied the 100 ML-thick closed film to further verify that our islands were not in the thin-film limit and did not show any lateral finite-size effects. As will be discussed in the next section, the closed film indeed displayed the same behavior as the islands mostly studied. Our preference of focusing on islands was based on two observations: (a) the closed films exhibited much dirtier surfaces (Fig. S3D), as more deposited material simply leads to more impurities that can segregate to the surface; (b) the screw dislocations found in the closed film, but not for the islands, can pin the magnetic structure, as was demonstrated for thick Dy films on W(110) (*51, 80*). Hence, SK-grown islands have a superior morphology and crystallinity, and from our comparison of differently sized islands and the closed film we could rule out any finite-size effects. Thus, we conclude that the SK-grown nanocrystallite islands fully reflect the structural, electronic and magnetic properties of bulk neodymium.

S2 - Real-space magnetization and corresponding Q-space images

Experiments were performed in two different home-built UHV-STM systems. The first system can be operated at two different stable temperatures, $T = 1.2$ K and $T = 4.2$ K, with an applied out-of-plane magnetic field up to 9 T. The second system operates at $T = 30$ mK and $T = 7$ K, with an in-plane magnetic field up to 4 T, and an out-of-plane magnetic field up to 9 T (*69*). Our systems allow the tip to stay on the same sample area while switching between the mentioned temperatures. As spin-polarized measurements require a stable drift-free tip-sample tunneling contact, we are neither able to acquire data

continuously while warming up or cooling down to the stable temperature regimes, nor can we stabilize the tunneling junction at temperatures above the previously mentioned temperatures. After a magnetic field sweep or temperature change, we need to stabilize the tunneling junction on the order of 60 min, before resuming an image on an identical area. Similarly, spatially dependent imaging cannot be performed during a magnetic field sweep due to similar stabilization arguments resulting from small changes in temperature, combined with the length of time it takes to acquire a typical image (120 min). Thus, aging experiments only contain images before and after magnetic field exposure, with varying exposure times.

Fig. S2A illustrates the surface of a typical Nd island, imaged with an out-of-plane polarized bulk Cr tip at V_S = 1 V. Note that for all STM topography images shown in the main text as well as the supplementary material, apart from a global plane subtraction no processing of the raw data was performed. The surface of these islands showed a distribution of surface impurities, which likely resulted from oxygen, carbon or hydrogen contamination (*52, 53*), in addition to features that were related to the underlying morphology of the W(110): substrate step edges were visible on the Nd surface because the atomic layer height for the two materials is different (*52*). Tunneling spectroscopy of the surface (Fig. 1C and Fig. S2I) revealed the expected surface state of Nd(0001), which is characterized by an exchange splitting into a majority peak visible below E_F and a minority peak above E_F, with an additional narrow peak at E_F *(54)*. Previous studies have measured the temperature dependence of the exchange splitting ΔE_{ex}, illustrating that the splitting persists far above T_N = 19.9 K (*27*). The slowly diminishing value of ΔE_{ex} above T_N is unusual compared to other lanthanide metals (*27, 49, 81*), which is another signature of strong local correlations in Nd (*26*). We note that the narrow peak at E_F has been seen on other lanthanides as well (*27, 53, 54*), i.e., there is no connection to the spin-Q glass behavior only found in Nd so far. Comparing spectra at T = 1.3 K and T = 40 mK, this resonance narrowed at lower temperature. Also, we did not see this feature strongly change in magnetic field. Therefore, we believe this feature is most likely related to a van Hove singularity. We note that images taken at a sample bias of 1 V (Fig. S2A) did not show any spin contrast. This is expected, as tunneling then occurs not only into the minority surface state but also bulk majority and minority states. Hence, the STM image is identical to that taken with a nonmagnetic tip.

In order to acquire spin contrast, we utilized a Cr bulk tip, which we cleaned by *in-situ* electron bombardment, and later prepared by tip pulsing until achieving an optimal out-of-plane contrast. We note that we could sometimes observe probes with a canted magnetization, but we have never observed probes with only a pure in-plane and stable magnetization. Zochowski *et al.* already pointed out that there is a tendency toward a simplified separation of spin order on the hexagonal vs. the cubic sites (*23*), whereas in fact: "It has been established that, below T = 10 K, the hexagonal sites have induced moments with components along the *c*-axis due to the ordered moments on the cubic sites and that the cubic sites have induced moments with components in the *c*-axis due to the ordered moments on the

hexagonal sites" (*23*). This statement is further supported by thermal expansion and magnetostriction data showing anomalies along the *c*-axis in the entire temperature range from 1 to 10 K. Hence, we expect that an out-of-plane polarized tip can map the out-of-plane component of the spin structure, irrespective of whether the surface is terminated by a hexagonal or a cubic layer. As STM probes the topmost layer, we have no means of determining what the termination of our surfaces is. Nevertheless, we point out that we measured islands of various thicknesses, sometimes including monolayer step edges. The magnetic structure was always observed to be comparable.

Constant-current SP-STM images near either peak of the exchange-split surface state using out-of-plane tips showed the magnetic pattern in real space that is overlaid with the topographic features (Fig S2B, C). While the topographic contrast was nearly identical at both imaging biases, the magnetic contrast was nearly fully inverted. This is a hallmark of spin polarization. To verify this, we also compared tunneling spectra from two different local points on the surface that showed opposing magnetic contrast (Fig. S2I). As expected, the red spectrum had a larger intensity of the majority peak below E_F compared to the blue spectrum, whereas the situation was reversed for the minority peak above E_F (*80, 82*). Tunneling into bulk states is negligible in the energy window governed by the surface state, because there is a bulk symmetry gap in the center of the surface-projected Brillouin zone. Thus, tunneling almost exclusively happens between the tip and the highly spin-polarized surface state, i.e., out of the majority state at negative sample bias and into the minority state at positive sample bias, respectively (*94, 95*). As a further evidence that the observed contrast was of magnetic origin, we present in Fig. S2J a constant-current STM image of an island acquired with a non-magnetic W tip, using the same stabilization parameters as in Fig. S2B (note that this image is from a different sample preparation where the surface impurity density was higher). No magnetic contrast could be observed with the W tip, as opposed to the Cr tip. The W tip could, however, be made spin-polarized by dipping the tip into Nd and thereby picking up a Nd cluster at the tip apex. Fig. S2K shows the exact same area as in (J) using such a Nd-terminated tip, which now showed the magnetic contrast of the surface. Due to the lack of knowledge about both the polarization and the behavior of the tip in magnetic field, we chose to use well-known bulk Cr tips for the rest of this study.

For the magnetization images introduced in the main text, we acquired SP-STM images at V_S = 200 mV and V_S = -150 mV, respectively (Fig S2B, C), and subsequently subtracted them from each other (Fig S2D). As a result of the subtraction process, the real-space magnetization images did not require any further processing (e.g. background correction or filtering), since both of the topography images have the same global slope. As the topographic contrast in both images was nearly identical, and the magnetic contrast was inverted, subtraction resulted in the magnetic contrast without the large-scale topographic features. This also revealed that that overgrown steps from the underlying W(110) interface did not affect the magnetic structure on the surface, as we did not observe any disturbance in the magnetic pattern correlating with the substrate step edges. We note that most atomic-scale impurities are still visible after

subtraction. However, this is an electronic effect rather than magnetic contrast, because the impurities influence the width and intensity of the much narrower majority state and the van Hove singularity more strongly than the much broader minority state, which leads to a bias-dependent apparent height of the impurities such that they do not cancel in the subtraction (*53*). For the Q-space images, we computed the Fast-Fourier Transform (FFT) of the real space images by using MATLAB, and we did not apply any post-processing, e.g. symmetrization or removal of intensity near $Q = 0$ that is caused by edge effects of the image, discussed in detail below (cf. section S3). The FFT intensity is always shown with square root scaling in inverted grayscale. All the Q-space images shown in this study have minimum 12 pixel per nm^{-1} resolution.

By comparing the Q-space images for the individual SP-STM images taken at each surface state energy (Fig. S2F,G) with the Q-space image of to the subtracted magnetization image (Fig, S2H), we illustrate that the features stemming from the magnetic structure were nearly identical. This is also true for images acquired in magnetic field (cf. Fig. S12). We note here that tips with a magnetization component in the plane of the sample led to certain observed **Q** vectors in a given image at one surface-state energy which was different compared to its surface-state partner image (see circles in Fig. S2).

In Fig. S3, we compare the topography, magnetization and Q-space images of a Nd island (A-C) with those of the ~100 ML closed film (D-F). Despite the fact that the closed film had a higher surface-defect density (D, see also Fig. 4 and the corresponding discussion in the main text) and a few screw dislocations, the magnetization image (E) clearly showed a multi-Q structure with locally varying short-range order but no globally ordered ground state, reminiscent of the image observed on the island (B). This was also reflected by the corresponding Q-space image (F), which qualitatively agreed well with that of the island (C). This confirms our conclusion of the previous section that SK-grown islands, despite their seemingly small size, fully reflect bulk magnetic properties.

S3 - Variation in local order and Q-state distribution

To determine the range of Q-pockets mentioned in the main text (Q_A, Q_B, and Q_C), we considered several Q-space images of the subtracted real-space magnetization images, measured at $T = 1.3$ K on several islands of similar dimensions without an external magnetic field. Various line-cuts along the $\bar{\Gamma}$-$\bar{M}$ direction of the Q-space images were produced in order to visualize the spectral weight of the **Q** vectors. Line-cut data (Fig. 1F, 5G, S13I) were flattened by subtracting a linear baseline, and smoothed by utilizing a Savitzky-Golay filter with 7-9 neighbors in order to reduce the background noise.

In Fig. S4, we utilized inverse FFT filtering at each identified Q-pocket and plot the resultant filtered magnetization images, where the overall intensity is related to the contribution of the selected Q states.

The images illustrate the large variation in spectral weight of each of the Q-pockets and that the underlying local order has various contributions from the named Q-pockets as schematically illustrated in Fig. 2B of the main text. In Fig. 1F of the main text, we show line-cuts of FFTs taken from smaller regions of the large-scale image illustrated in Fig. 1D. Each of these regions, plotted in Fig. S5, primarily showed one type of distribution of Q states.

Here, we would like to comment on the resolution of the Q-space images in relation to the observed widths of features. In brief, the resolution of a 2D FFT depends on a number of factors, e.g. the number of pixels in the image compared to the wavelength of the features extracted. As the FFT is performed always on finite-size images with a finite number of pixels, there are artifacts, well known in the STM community that can arise. For example, the enhanced intensity near $Q = 0$ in the FFT is a result of finite-size effects, and this intensity must be disregarded. Usually, this is cropped out of images, but we preferred to provide unprocessed raw data. Most importantly, the interpretation of reciprocal peak widths as known from neutron diffraction or XRD, cannot be translated one-to-one to Q-space maps, extracted from SP-STM. Spot broadening in diffraction experiments is commonly interpreted as an effect of finite sample or domain size. To exemplify that our Q-space maps have to be interpreted differently, we point out the examples shown in Fig. 1 of the main text: the smaller images in Fig. 1G and Fig. S5 were simply cropped from the larger image (Fig. 1D). The FFT of the larger image, i.e. larger spatial area, showed a much broader and smeared out intensity (Fig. 1E), compared to the cropped images (Fig. S5D-F, J-L). The cropped images showed much more well-defined Q-vectors, but with varying magnitudes and spectral intensities. In essence, if one were to "sum" these smaller regions up, a broadened intensity would be obtained, which is characteristic of the spin-Q glass landscape we highlight in the paper. That said, the discussed broad features were real and not due to limited resolution of our FFTs. This can also be deduced from the magnetic field-dependent data where features sharpened along the high-symmetry direction (angular direction), while the magnitude of the Q-vectors smeared out (radial direction). The FFTs simply reflect what is seen in the real space images, namely that the wavelengths are not uniform. Magnetization images showed a spatially dependent spectral weight of Q states, as illustrated in the FFTs of Fig. 1E of the main text and Fig. S5.

S4 - Comparison of surface and bulk magnetic moments

STM is a surface-sensitive method, and therefore care has to be taken before one can conclude that it reflects the bulk magnetization. In order for the surface layer(s) of a magnetic material to possess a different magnetic structure than the bulk, it is first of all necessary that the magnetic state (as reflected by moments and exchange interactions) is drastically different at the surface layers. Secondly, these exchange interactions need to be sufficiently dominant in order to overcome the exchange coupling between atoms at the surface and atoms deeper into the bulk. In order to investigate the difference in

8

magnetism of the bulk and the surface of Nd we performed calculations, as described in the methods section, of two surface terminations of the Nd crystal, with either a cubic layer as the surface layer or the hexagonal layer as the surface layer. The former calculation employed a slab geometry with 13 atomic layers and the latter calculation employed a slab with 11 layers. In each calculation we introduced a vacuum region of 11 Å. The structures were relaxed with respect to geometry, using force minimization, and it was found that the surface layer of the hexagonal termination relaxed 2.5% inward, while the subsurface layer relaxed 6% outward. For the cubic termination the surface layer relaxed 2.2% inward while the subsurface layer relaxed 5.8% outward.

The magnetic moments of the two surface calculations are shown in Table S2. Here we report the total moment of the surface (1st) and subsurface (2nd) layer. These moments should be compared to those of the bulk, which are also presented in Table S2. It may be seen that the total moment was similar for the surface layers (of either termination) and the bulk values. In addition, we found that the bulk value of the total magnetic moment was reached 3-4 atomic layers below the surface (data not shown). The microscopic reason why the magnetic state is bulk-like just a few layers below the surface can be traced back to the electronic structure, that in essentially all materials investigated by density functional theory, it is known to become bulk-like just a few atomic layers below the surface (96). This has been discussed in terms of the 'nearsightedness' of density functional theory (97).

S5 - Spin simulations and Q-state energetics

The spin simulations presented in the main text were performed using both Monte Carlo simulations (MC) and atomistic spin dynamics simulations (ASD), using the UppASD software (71). We used the parameterized spin Hamiltonian $H = -\sum_{i \neq j} J_{ij} \boldsymbol{e}_i \cdot \boldsymbol{e}_j$ based on unit vector spins $\boldsymbol{e}_i$ and exchange couplings J_{ij} calculated from DFT and the RSPt software (70), as described in the methods section. The ground state of the two methods was the same, and for equilibrium properties the methods can be used interchangeably. The ASD methodology gives a correct description of the timescale for the dynamical processes in the system and thus a possibility to control the rates of relaxation processes. For the MC simulations we used the Metropolis-Hastings algorithm (98) to obtain states as close to the ground state as possible. Given the glassy nature of the system, the efficiency of this procedure depended strongly on the relaxation protocol, i.e. how the temperature was varied during the simulations.

The ASD simulations were performed by evaluating the Landau-Lifshitz-Gilbert equation of motion for each atomic moment $\boldsymbol{m}_i$ in the effective site-dependent field $\boldsymbol{B}_i$ according to

$$\frac{d\boldsymbol{m}_i}{dt} = -\gamma \boldsymbol{m}_i \times \boldsymbol{B}_i - \gamma \frac{\alpha}{m_i} \boldsymbol{m}_i \times (\boldsymbol{m}_i \times \boldsymbol{B}_i)$$

where γ is the gyromagnetic ratio, and α the Gilbert damping parameter that determines the rate of dissipation of energy from the spin system. Thermal effects were included in the ASD method by means of Langevin dynamics where a stochastic noise term is added to the effective magnetic field $\boldsymbol{B}_i$. All simulations were done with the UppASD software (*71, 99*) and the algorithms used are given in full detail in Ref. (*72*).

For the determination of Q states from the static correlation functions $S(\boldsymbol{Q})$, displayed in Fig. 3D in the main text, we followed a simulated cooling protocol where the temperature was decreased from $T =$ 20 K (which is above the ordering temperature) with steps of $\Delta T = 5$ K while performing 10^5 Monte Carlo sweeps at each temperature. The correlation functions were then sampled using 10^5 ASD steps with a Gilbert damping parameter of $\alpha = 0.01$ and a time step of 10^{-16} s. The Q-space correlation function $S(\boldsymbol{Q})$ was obtained as the Fourier transform of the real-space trajectories of the system, which were sampled every 100th time step.

The energetics of the single-Q spirals, displayed in Fig. 3B in the main text, were evaluated by constructing helical spin spirals for given wave vectors $\boldsymbol{Q}$, where the plane of rotation of the spins was defined to be perpendicular to the wave vector, i.e. the magnetization of the spin-spiral has both in-plane and out-of-plane components. The spatial magnetization profile for a single-Q spin spiral was constructed as:

$$\boldsymbol{m}(\boldsymbol{r}, \boldsymbol{Q}) = m\,[\,\sin(\boldsymbol{r} \cdot \boldsymbol{Q})\,\hat{\boldsymbol{n}} + \cos(\boldsymbol{r} \cdot \boldsymbol{Q})\,\hat{\boldsymbol{z}}]$$

where $\hat{n} = \hat{Q} \times \hat{z}$ so that the in-plane component of the magnetization is perpendicular to the $\boldsymbol{Q}$ vector. The energy of each single-Q spiral was then obtained by evaluating the spin Hamiltonian defined above. We note that since only isotropic Heisenberg exchange interactions were included in the Hamiltonian, the energy of a single-Q spin spiral did not depend on the orientation of the plane where the spins rotate, i.e., cycloidal and helical spin-states were degenerate for the same $\boldsymbol{Q}$ vector.

S6 - Periodicity of the spin-spiral energy landscape

The single-Q spin spiral energy landscape $E(\boldsymbol{Q})$, which is presented in Fig. 3B in the main text, has a periodicity that might seem confusing: when going along the Σ symmetry line (Γ-M-Γ), it would seem that $E(\boldsymbol{Q})$ is not equivalent for the two Γ points. This behavior can, however, be explained from the dhcp structure, in particular by the difference between the positions of the atoms on the hexagonal and the cubic sublattices. In the Figs. S6-7, we plot schematically how the spins of the different sublattices rotated in the presence of a wave vector $\boldsymbol{Q}$. For simplicity, we considered a ferromagnetic reference state but the analysis holds for the ground state magnetic structure of bulk dhcp Nd, where the moments of the

10

different sublattices are rotated 90 degrees with respect to each other as well. In the schematic figures, the moments of the two inequivalent sites for the cubic sublattices were colored with different shades of red, while the moments on the hexagonal sublattices were colored blue, i.e., using the same color representation as the crystal structure displayed in Fig. 3A in the main text.

S7 - Decomposition of the simulated magnetic structure for various *Q* vectors

The schematic magnetization images shown in Fig. 1H in the main text were obtained as linear combinations of spin spirals with distinct *Q* vectors having different wavelengths (Q_A = 1.5 nm^{-1}, Q_B = 3.0 nm^{-1}, and Q_C = 5.0 nm^{-1}), inspired by the observed Q-pockets. This is analogous to an inverse Fourier transform of the selected *Q* vectors, with the difference that for the construction of the spirals used for the images in Fig. 1H, the magnetization of the resulting multi-*Q* spin spirals was rescaled so that the norm of the magnetization was kept constant. A proper linear combination of single-*Q* spirals would otherwise result in longitudinal fluctuations, i.e. changes of the local magnetic moment magnitudes; but in order to stay consistent with our unit-vector based Hamiltonian, we here enforced constant moment magnitudes. In Fig. S8, we illustrate the resultant site-dependent magnetization for various *Q* vectors taken from the calculation illustrated in Fig. 3 in the main text.

As a supplement to the schematic picture in Fig. 2B in the main text, we simulated a quenching, i.e. a rapid cooling of the system going from T = 7 K to T = 0 K, using Metropolis MC simulations (Fig. S9). The quenching protocol ensured a correct description of the long-range magnetic structure of the high-temperature state while removing local fluctuations. From this rapidly cooled system several single-*Q* and multi-*Q* states were visible, where the spectral weight varied spatially without clearly defined domain walls as in typical multi-*Q* systems (*58*). These results were comparable to the experimental observations in Figs. 1 and 5.

S8 - Calculation of the autocorrelation function

The results for the autocorrelation function $C(t_w, t) = \langle m_i(t + t_w) \cdot m_i(t_w) \rangle$ presented in the main text were obtained from ASD simulations following the Landau-Lifshitz-Gilbert equation described in preceding sections. The procedure was to start with a completely random distribution of magnetic moments, whose directions evolved with time. For a selection of waiting times t_w, separate single-site correlations $m_i(t + t_w) \cdot m_i(t_w)$ were sampled during the simulation times, t, and averaging was performed over all Nd sites. Here a large value of the Gilbert damping parameter $\alpha = 0.5$ was used in order to capture the relaxation dynamics efficiently. While such a large damping can be seen as unrealistic, earlier ASD

simulations on spin glass systems have shown that the glassy relaxation dynamics is captured for all considered choices of damping values (*10*). For comparison, autocorrelation measurements were also performed for simulations with lower damping values as well as when using the Metropolis MC algorithm, and all simulations showed glassy behavior of the autocorrelation functions.

In order to further establish the glassy behavior of the dhcp Nd system, and to also confirm that the short time scales available from the atomistic simulations are still long enough to identify different types of relaxation dynamics, additional simulations on dhcp model systems were performed. In addition to the proper bulk dhcp Nd system, we here considered model spin Hamiltonians containing interactions from only the nearest, next-nearest, and third-nearest neighbors. For these short-ranged Hamiltonians we then modified the interactions to be either (a) with the same magnitude of the dhcp Nd interactions but with positive sign to all interactions, giving a ferromagnetic ground state; (b) same magnitude of the dhcp Nd interactions but with negative signs to all interactions, giving a frustrated/antiferromagnetic ground state; or (c) random exchange interactions following a Gaussian distribution, renormalized to mimic the same order of magnitude of the exchange interactions of dhcp Nd, giving an Edwards-Anderson like model (*1, 2*). The dynamics of all model Hamiltonians were simulated using ASD with a Gilbert damping factor of 0.5 and for system sizes consisting of a 24x24x24 repetition of dhcp cells. We note that this differs from the 32x32x32 size used for the autocorrelation simulations presented in the main text.

The simulations, displayed in Fig. S10, showed that for the ferromagnetic model Hamiltonian, the autocorrelation function converged to a finite value rapidly as expected with the large Gilbert damping used. The antiferromagnetic model also showed a rapid convergence of the autocorrelation function. In contrast, the Edwards-Anderson model showed a relaxation behavior closer to that of the spin-Q glass behavior of dhcp Nd presented in Fig. 3C in the main text. It is also evident from Fig. S10 that there was a distinct difference of the autocorrelation functions for the glassy systems (spin-Q and Edwards-Anderson) compared to the non-glassy (ferro- and antiferromagnetic) systems which was clearly visible for the simulation times available from the ASD simulations.

S9 - Magnetic field dependence of spin-Q glass

Fig. S11 illustrates all the magnetic as well as Q-space images in varying out-of-plane magnetic field that were utilized for the line-cuts displayed in Fig. 5G of the main text. With increasing out-of-plane magnetic field, we observed that the Q_A and Q_B pockets merged, while the spectral weight more broadly distributed in the Q_C pockets. These features were independent of the subtraction method, as shown in Fig. S12, where we compared the raw SP-STM images and their respective FFTs at the two surface-state energies, for two different magnetic fields. Comparing Figs. S12C,D with Fig. S11F as well as Figs. S12G,H with

Fig. S11Q, each image showed the same features as the corresponding subtracted image. Similar trends were seen for in-plane magnetic fields.

Fig. S13 illustrates a region measured at T = 40 mK, with a higher defect density (ca. 0.015 ML). The overall spectral weight collapsed onto the axis perpendicular to the applied field direction, which is indicated in the figure. The same qualitative behavior has also been observed in field-dependent neutron diffraction studies with magnetic fields applied close to one of the basal high-symmetry directions (*22-24*). At intermediate fields, a variation in spectral weight was observed, similar to the out-of-plane experiments. This spectral weight broadened in higher applied fields, as illustrated by the line cuts shown in Fig. S13I. We note here that due to the high defect density, the FFTs of this region were noisier in comparison to the out-of-plane data.

S10 - Aging in Nd(0001)

The distinguishing feature of spin glasses is the presence of aging dynamics. The most traditional definition of aging, as inspired by experimental evidence, is characterized by magnetization states which never fully relax resulting from the presence of multiple relaxation time scales, regardless of the waiting time (cf. section S8). This relaxation behavior can span many orders of magnitude in time, as exemplified by the magnetic alloys such as Cu-Mn (*3, 100*), which exhibits glassy dynamics below a particular freezing temperature above which the material is paramagnetic.

Aging behavior in out-of-plane magnetic fields is extensively discussed in the text. We also saw aging behavior for applied in-plane magnetic fields. Fig. S14 illustrates a region measured at T = 40 mK. We note that in the pristine state (Fig. S14A), there were predominately Q-states along one orientation. As this area was imaged near an edge of the island, we suggest that magnetostrictive strain might have locked the Q states into this direction during the initial zero-field cool-down of the sample. However, after applying an in-plane field sweep, the Q states completely randomized their orientation (Fig. S14B), uninfluenced by the island edge. This illustrated the negligible impact of the island edges to the energy landscape. After subsequent in-plane field sweeps, we saw similar behavior as in out-of-plane fields, in which the spectral weight was randomly changed and showed no preferential distribution. Moreover, to compare the behavior with the above data taken at T = 1.3 K, we also performed a field sweep in an out-of-plane field at T = 40 mK, on the same area (Fig. S14E), and observed the same aging behavior that is illustrated in the main text. Therefore, we conclude that the aging behavior was independent of the applied field direction.

13

S11 - Temperature dependence of spin-Q glass state

Fig. S15 illustrates the magnetic field dependence and resultant aging at T = 4.2 K. Comparison of magnetization images taken at T = 1.3 K and T = 4.2 K, as well as aging behavior for the Q-pockets are discussed in detail in the main text. Imaging the same region at T = 4.2 K in out-of-plane magnetic fields also illustrates the same trends in the spectral weight in other regions of Q-space similar to the observations at T = 1.3 K. Namely, the spectral weight broadened along the other pockets without the appearance of any favorable Q state.

Previous neutron diffraction data illustrates the emergence of new Q states with decreasing temperature, starting at T < 19.9 K, down to T = 1.8 K. Similarly, we performed temperature-dependent measurements. At T = 7 K (Fig. S16A, C), we observed primarily Q states at high Q values with an absence of longer-range ordered states as observed at T = 1.3 K. Images of the same region at T = 40 mK (Fig. S16B, D) illustrated a behavior similar to that observed at T = 1.3 K, with the emergence of spectral weight in the Q_A pockets which are absent in images at T = 7 K. Moreover, we note that we did not observe any new Q states at T = 40 mK, in comparison to images taken at T = 1.3 K, suggesting that either the system was completely frozen into a finite number of Q states, or that fluctuations persisted down to lower temperature, inhibiting certain Q states to freeze.
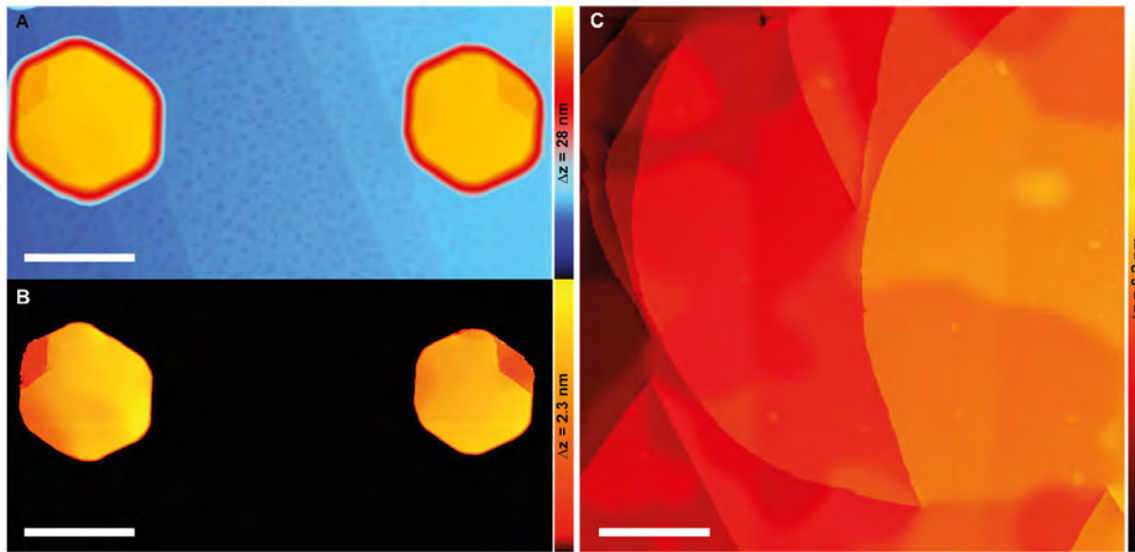
Fig. S1. Nd(0001) morphology of islands and closed films.

(**A**) Constant-current STM image of a Nd film on W(110) (~15 ML deposition), after annealing to 700°C, leading to Stranski-Krastanov growth of nearly flat-top islands (> 50 ML) on a Nd wetting layer (V_S = 1 V, I_t = 20 pA, scale bar = 150 nm). (**B**) Same image as in (A) with reduced vertical scale bar to show the atomic-scale surface morphology. Steps are visible due to locally varying Nd layer thickness as well as overgrown atomic steps at the Nd-W interface. No line defects or any other signature of dislocations are visible. (**C**) Constant-current STM image of a ~100 ML Nd film on W(110) after annealing to 700°C, leading to an extended, closed Nd film with relatively homogeneous thickness distribution (V_S = 1 V, I_t = 20 pA, scale bar = 150 nm). Several screw dislocations can be identified.
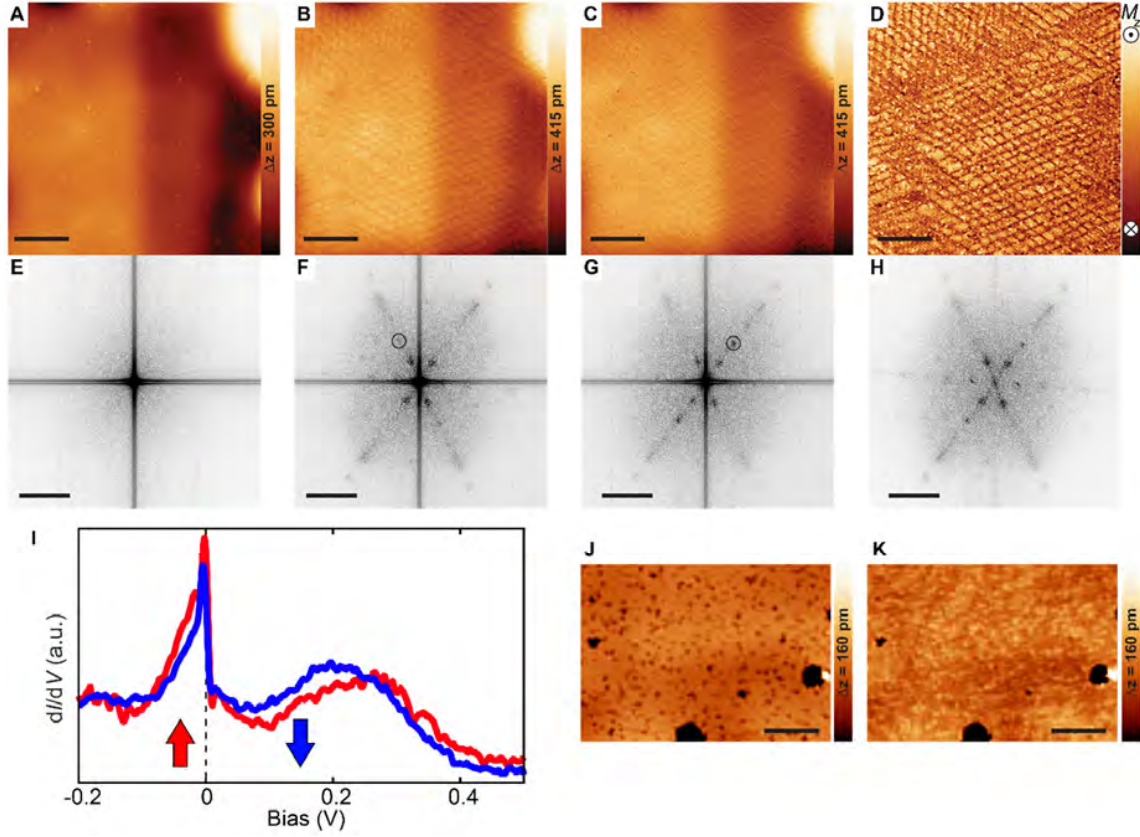
15

Fig. S2. Magnetization imaging method
(**A-C**) Topography images at constant-current mode with various sample biases; (A) at $V_S = 1$ V, $I_t = 200$ pA showing the morphology of the island surface; (B) at $V_S = 200$ mV, $I_t = 200$ pA and (C) at $V_S = -150$ mV, $I_t = 200$ pA both containing also magnetic information (scale bar = 30 nm). Magnetic contrast in the images measured at the minority (B) and the majority (C) surface state exhibits contrast reversal. (**D**) Magnetization image obtained by subtracting the minority image (B) from the majority image (C), revealing the magnetic structure of Nd(0001) surface. (**E-H**) Q-space images of the real-space images in (A-D) obtained by FFT (scale bar = 3 nm^{-1}). (**I**) dI/dV spectra acquired on two different points, showing opposite magnetic contrast on the surface ($V_{stab} = 1$ V, $I_{stab} = 300$ pA, $V_{mod} = 2$ mV; $T = 1.3$ K). (**J**) Constant-current STM image of a surface region probed with a non-magnetic W tip at $V_S = 200$ mV, $I_t = 200$ pA (scale bar = 15 nm). (**K**) The exact same area as in (J) imaged after picking up a magnetic Nd cluster by dipping the W tip gently into another Nd island, illustrating the magnetic patterns in the real space on top of the topographic features ($V_S = 200$ mV, $I_t = 200$ pA, scale bar = 15 nm).
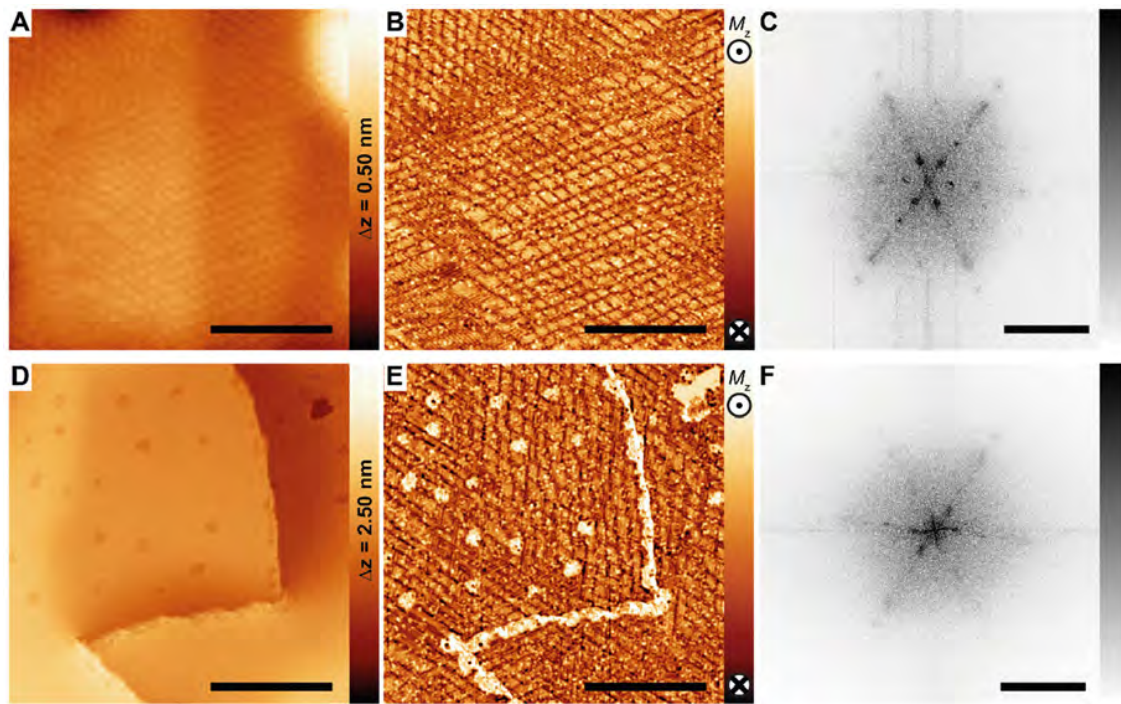
16

Fig. S3. Influence of magnetic structure on sample morphology.
(**A**) Topography of the surface of the Nd island shown in Fig. S2, which has an average thickness of 60 ML (V_S = 200 mV, I_t = 20 pA, scale bar = 50 nm). (**B**) Magnetization image of the same area shown in (A). (**C**) Corresponding Q-space image of the magnetization image in (B) (scale bar = 5 nm^{-1}). (**D**) Topography of the surface of a closed ~100 ML thick Nd film. Note the five times larger z-range compared to (A) (V_S = 200 mV, I_t = 20 pA, scale bar = 50 nm). (**E**) Magnetization image of the same area shown in (D). (**F**) Corresponding Q-space image (scale bar = 5 nm^{-1}) of the magnetization image in (E).
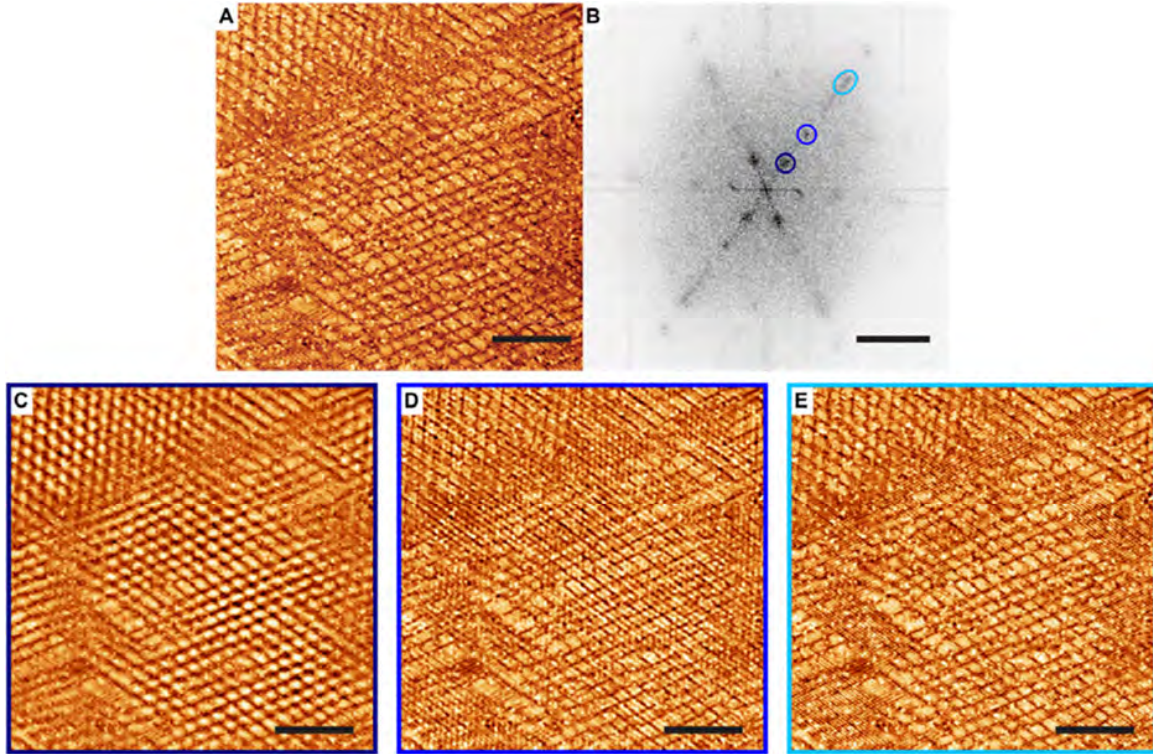
Fig. S4. Spectral decomposition of Q-pockets in real space.

(**A**) A magnetization image of the Nd(0001) surface, showing the spatially complex magnetic structure with superposition of different Q-states in different regions (scale bar = 30 nm, I_t = 200 pA). (**B**) Q-space image of the magnetization image in (A) (scale bar = 3 nm^{-1}). (**C-E**) Spectral decomposition maps obtained by superimposing the Q-states marked in (B) on the magnetization image in (A). By this way, real-space structure and spatial distribution of each Q-pocket can be visualized, revealing that not only the locations that are present but also the relative intensities are different.
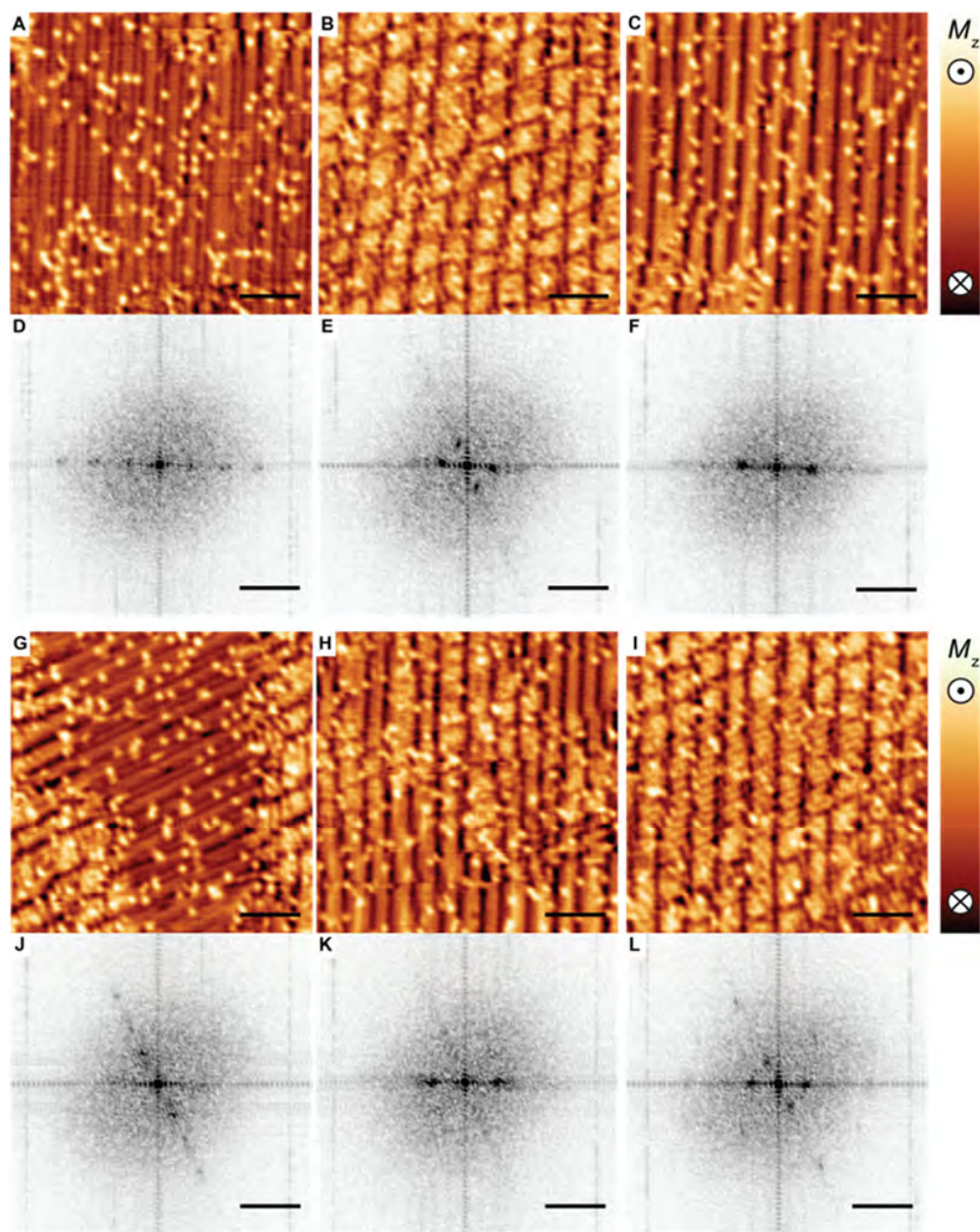
Fig. S5. Locally ordered states.
(**A**-**C**, **G**-**I**) Magnetization images showing different spatial regions of Fig.1D in the main text (scale bar = 10 nm, I = 200 pA). (**D**-**F**, **J**-**L**) Corresponding Q-space images revealing the local order, characterized by superposition of Q states (scale bar = 3 nm^{-1}).
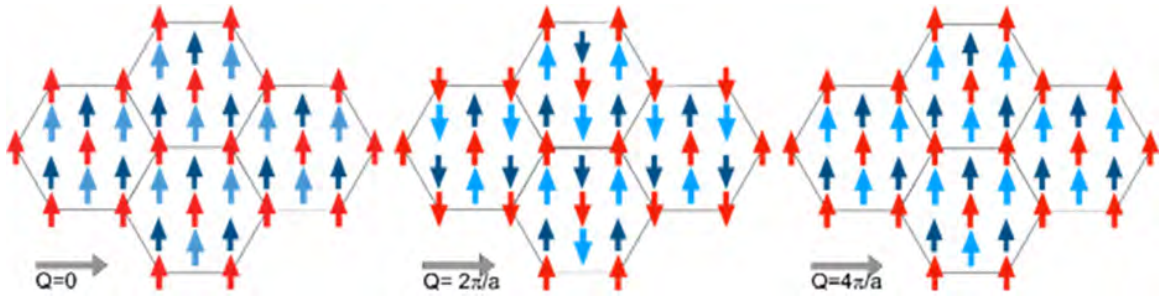
Fig. S6. Brillouin zone Γ-K.

Spin rotations for Q vectors along the direction of the grey arrow. Colors refer to the sublattice affiliations of the moments (red = hexagonal, blue = cubic). For $Q = 0$ (Γ, left panel), all moments are aligned ferromagnetically. A spiral with $Q = 2\pi/a$ (middle panel) results in a collinear antiferromagnetic state, while increasing the wave vector to $Q = 4\pi/a$ gives the original ferromagnetic state (right panel). For wave vectors along this direction, the periodicity is thus $4\pi/a$.
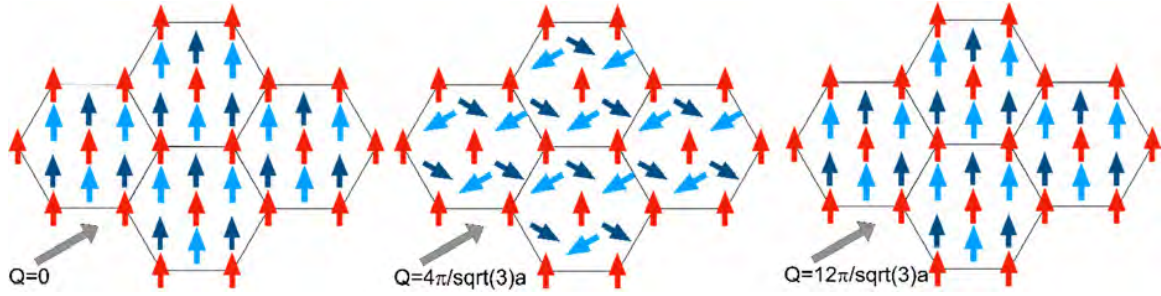
Fig. S7. Brillouin zone Γ-M.

Spin rotations for Q vectors along the direction of the grey arrow. For $Q = 0$ (Γ, left panel), all moments are aligned ferromagnetically. A spiral with $Q = 4\pi/\sqrt{3}a$ (middle panel) results in a non-collinear antiferromagnetic state where the moments of each hexagonal sublattice are rotated by 120 degrees with respect to the other sublattices, and all moments on the cubic sites are ferromagnetically aligned. In order to obtain the original ferromagnetic state for all sublattices, the wave vector needs to be increased to $Q = 12\pi/\sqrt{3}a$ (right panel). For wave vectors along this direction, the periodicity is thus longer for the dhcp structure than for the hcp structure.
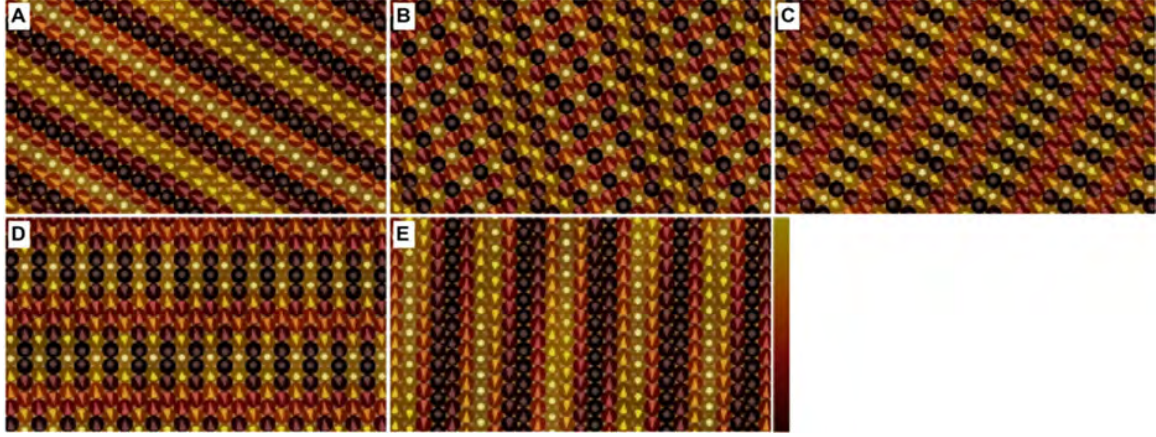
Fig. S8. *Q* vector decomposition of the calculated real-space magnetization.

Schematic depiction of the spin structure, where the directions of the cones refer to the magnetization direction, and the color contrast refers to the projected out-of-plane magnetization (colored spheres) obtained as the inverse Fourier transforms of the most significant $S(\mathbf{Q})$ signals from the ASD/MC simulations. All structures are characterized by a single $\mathbf{Q}$ vector which is (**A**) $\mathbf{Q} = 2\pi/a$ [0.22, -0.13, 0.00]; (**B**) $\mathbf{Q} = 2\pi/a$ [0.24, -0.40, 0.00]; (**C**) $\mathbf{Q} = 2\pi/a$ [0.44, -0.39, 0.00]; (**D**) $\mathbf{Q} = 2\pi/a$ [-0.10, -0.85, 0.00]; and (**E**) $\mathbf{Q} = 2\pi/a$ [0.02, -0.22, 0.00], where a is the lattice parameter for dhcp Nd.
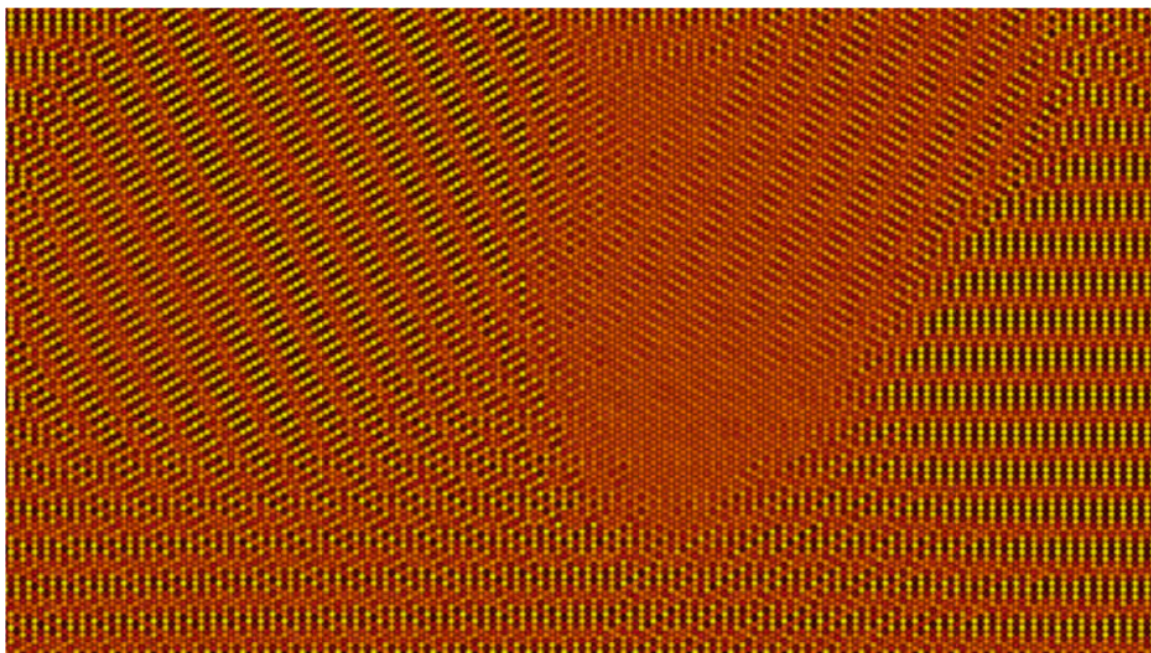
Fig. S9. Monte Carlo simulated results of a rapid cooling from 7 K to 0 K.

Results from spin dynamics simulations of bulk Nd as parameterized by *ab initio* exchange interactions, using Metropolis MC simulations.
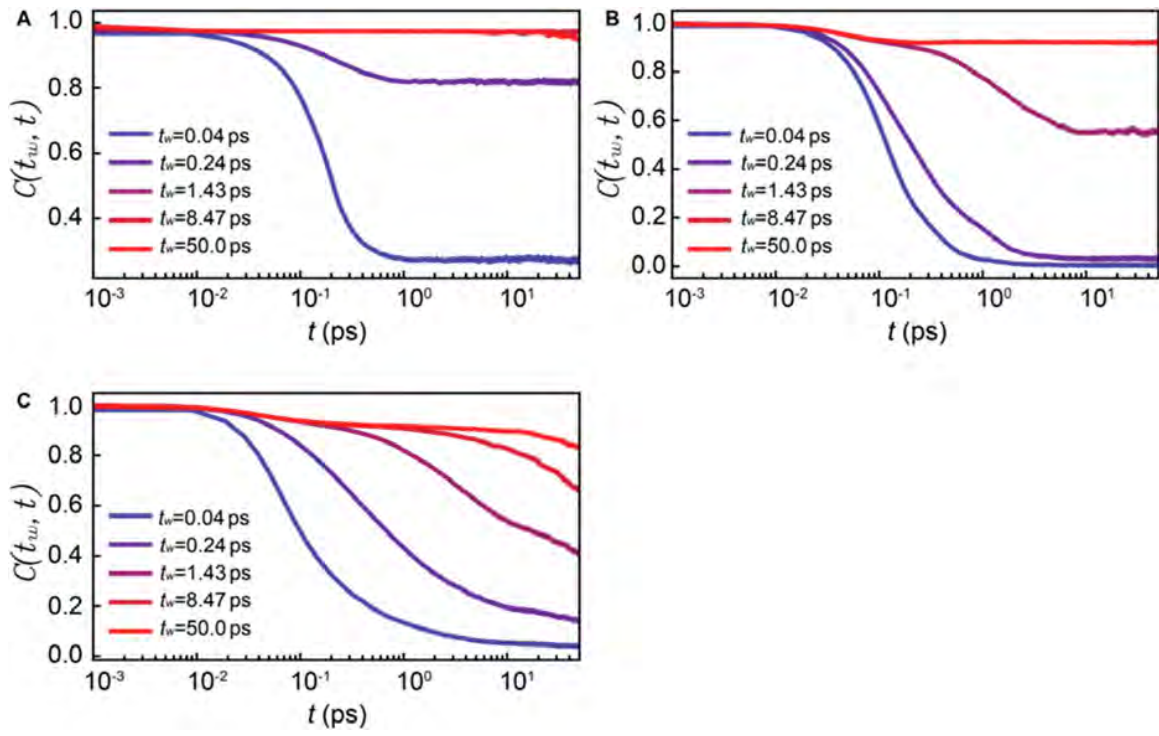
Fig. S10. Autocorrelation and aging.
Autocorrelation behavior showing the simulated relaxation dynamics at $T = 1$ K for (**A**) the ferromagnetic model, (**B**) the antiferromagnetic model, and (**C**) the Edwards-Anderson like model.
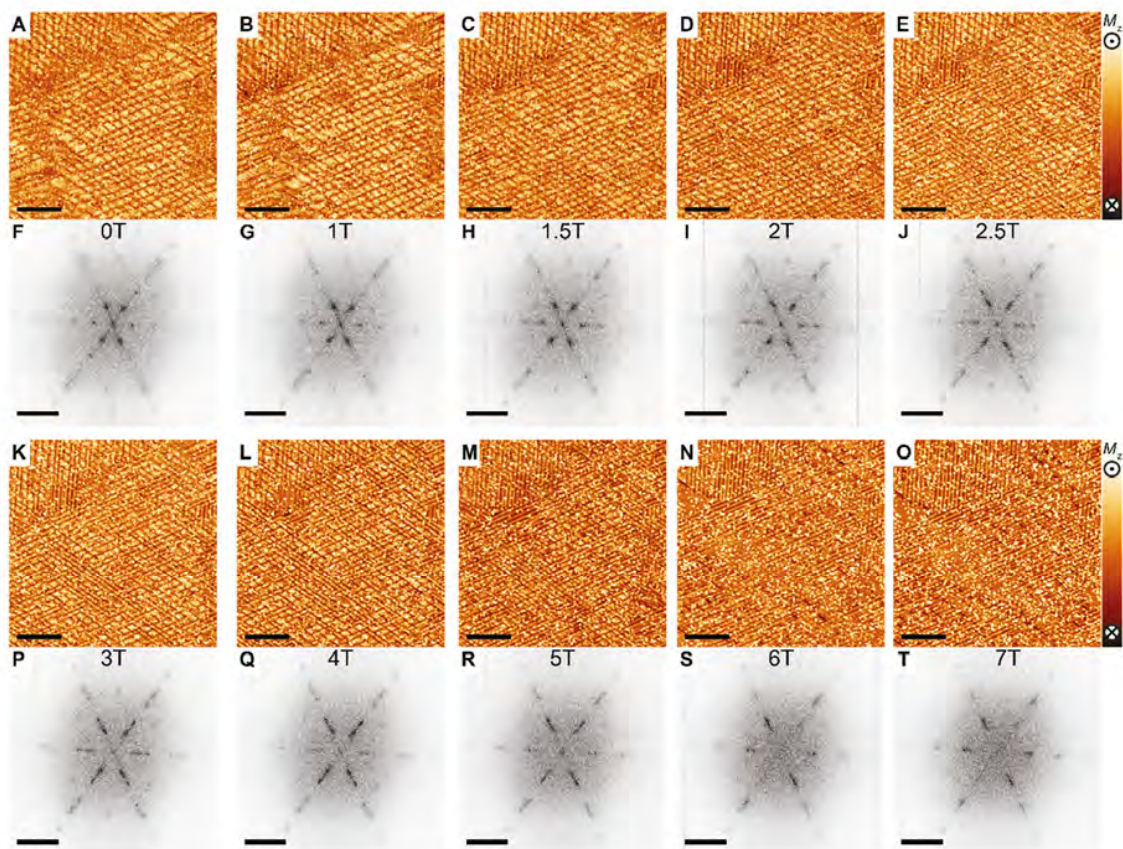
Fig. S11. Out-of-plane magnetic field evolution of the spin-Q glass state.

(**A-E**, **K-O**) Magnetization images of the same area measured in various out-of-plane magnetic fields at T = 1.3 K (scale bar = 30 nm, I_t = 200 pA). (**F-J**, **P-T**) Corresponding Q-space images of the magnetization images (scale bar = 3 nm^{-1}). All images are plotted with the same contrast.
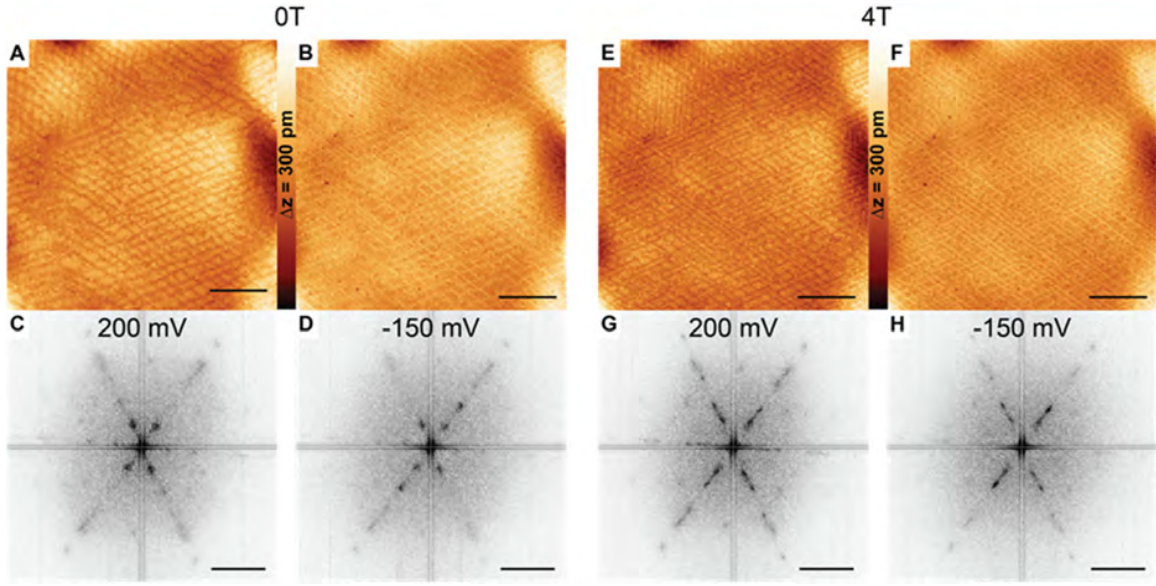
Fig. S12. Magnetic field dependence of spin contrast at surface-state energies.

(**A**, **B**) Constant-current SP-STM images measured at V_S = 200 mV, I_t = 200 pA and V_S = -150 mV, I_t = 200 pA at T = 1.3 K in B = 0 T. (**E**, **F**) The same area imaged in B_z = 4 T, at the same two bias voltages (scale bar = 30 nm). (**C**, **D**, **G**, **H**) Corresponding Q-space images of the images above, which can be compared to Fig. S11F and Fig. S11Q, respectively (scale bar = 3 nm^{-1}).
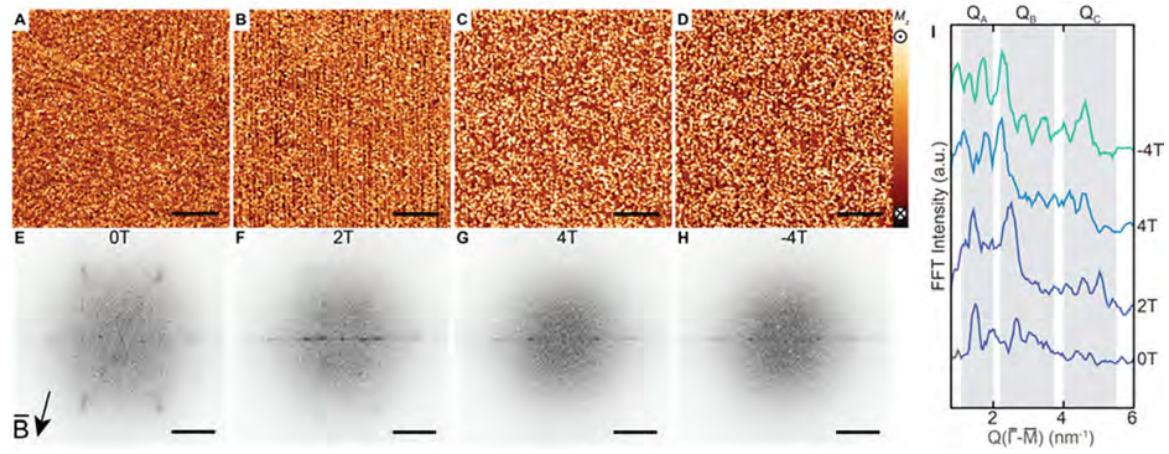
Fig. S13. In-plane magnetic field evolution of the spin-Q glass state.

(**A-D**) Magnetization images of the same area in various in-plane magnetic fields at T = 40 mK (scale bar = 30 nm, I_t = 200 pA) and (**E-H**) corresponding Q-space images of each image above (scale bar = 3 nm^{-1}). In-plane magnetic field is rotated 15º with respect to the y-axis of the STM images (cf. arrow in (E)). The sign of the magnetic field value defines the direction of the field. (**I**) Line-cuts along $\bar{\Gamma}$-$\bar{M}$ of Q-space images.
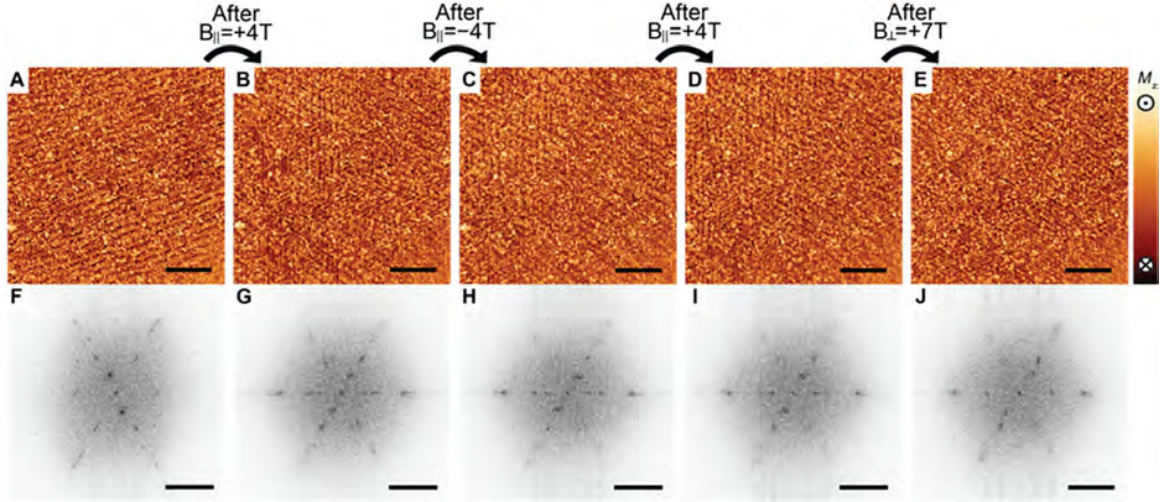
Fig. S14. Aging of the spin-Q glass state in magnetic field with various directions.
The measurements were taken at $T = 40$ mK, at a location close to the edge of a Nd island, which is presumably why the pristine state (**A**) has Q states locked mostly along one high-symmetry direction. (**B-D**) Series of in-plane field aging experiments measured on the exact same area as the pristine state ($t_i = 10^3$ s for each magnetic field). (**E**) Out-of-plane aging of the same area ($t_i = 10^3$ s) for comparison with the aging experiments at $T = 1.3$ K (cf. Fig. 6) (scale bar = 30 nm, $I_t = 200$ pA). (**F-J**) Corresponding Q-space images of the images above (scale bar = 3 nm^{-1}).
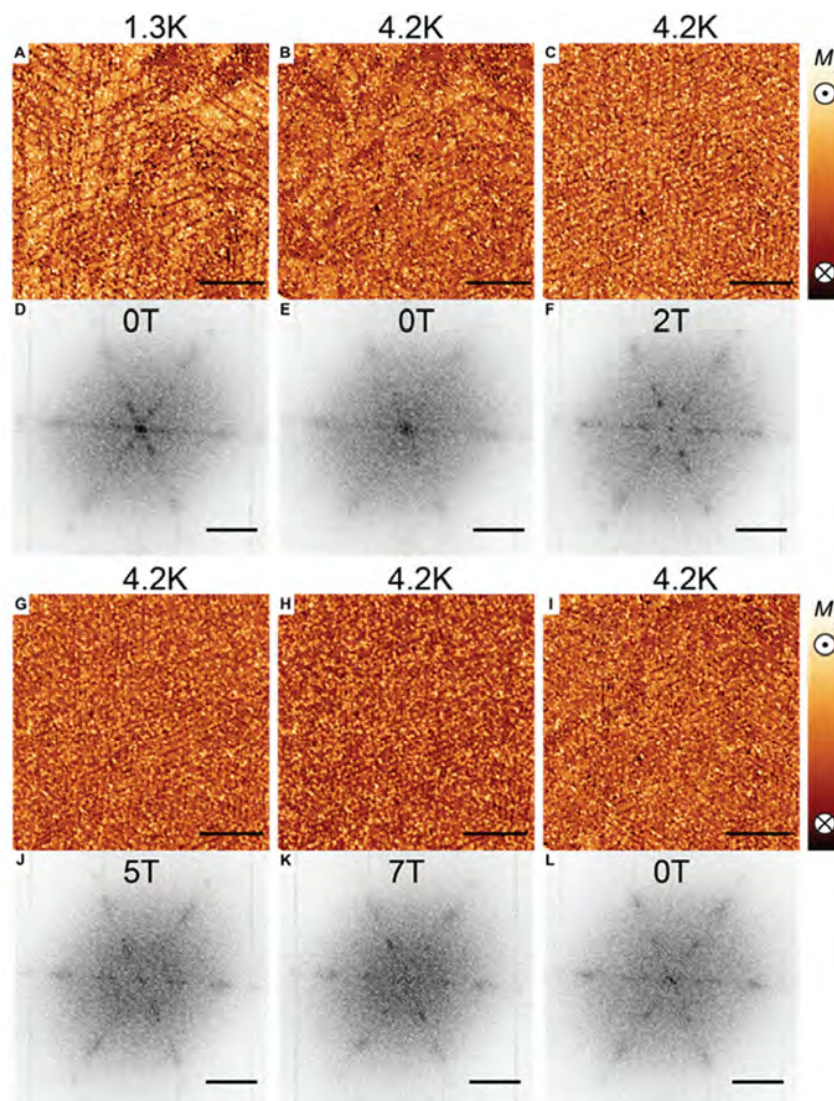
Fig. S15. Temperature dependence of the Q-pockets in magnetic field.

Magnetization images of the exact same area (**A**) at $T = 1.3$ K in $B = 0$ T and (**B**, **C**, **G-I**) at $T = 4.2$ K in various out-of-plane magnetic fields (scale bar = 30 nm, $I_t = 200$ pA). (**D-F**, **J-K**) Corresponding Q-space images of the images above (scale bar = 3 nm^{-1}). Warming up the surface from 1.3 K to 4.2 K results in depopulation of the Q_A pocket. Similar out-of-plane magnetic field dependence and aging behavior is observed at $T = 4.2$ K for the other Q-pockets. The magnetization image in (I), measured after magnetic field-dependent measurements, is the aged state of the pristine state in (B) ($\tau_i = 10^5$ s at above 1 T).
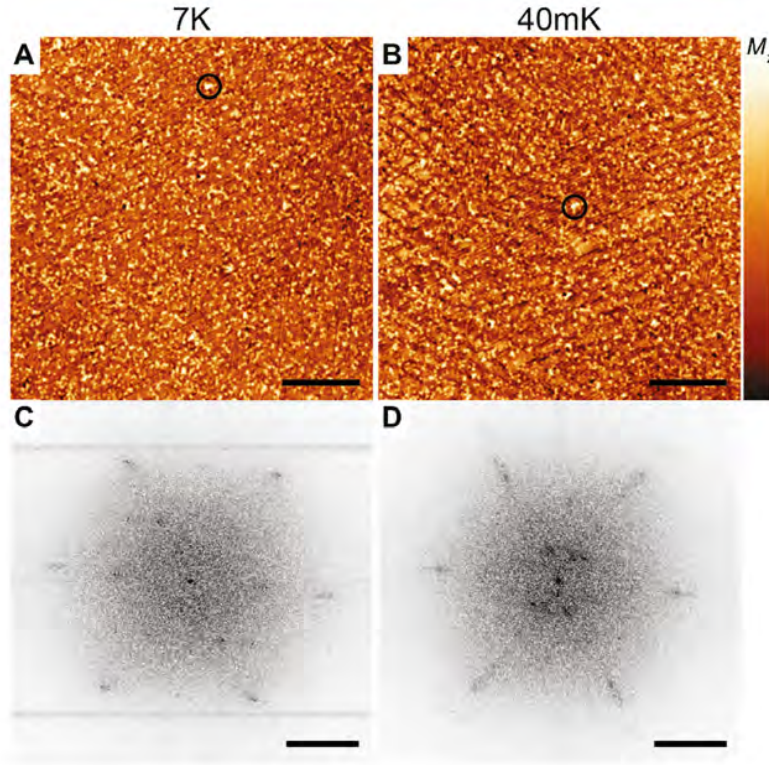
Fig. S16. Temperature dependence of spin-Q glass state.
Magnetization images of the same area (**A**) at $T = 7$ K, (**B**) at $T = 40$ mK (scale bar = 30 nm, $I_t = 200$ pA), and (**C**, **D**) corresponding Q-space images of the images above (scale bar = 3 nm^{-1}). The surface shows fewer but more well-defined Q states at $T = 7$ K. The absence of spectral weight in the Q_A pocket at higher temperature is similar to the observation at $T = 4.2$ K.

Table S1. Impurity concentration of the Nd source material.

Elemental analysis (weight and atomic ppm, elements with <1 ppma not shown) as provided by Ames Laboratory. The sum of all rare-earth impurities (including Y) is 18.2 ppma, that of all 3d elements 0.9 ppma.

Element	Concentration		Element	Concentration	
	(ppm wt.)	(ppma)		(ppm wt.)	(ppma)
O	257	2316	Pr	3.5	3.6
C	117	1704	Y	2.2	3.6
N	319	319	Si	0.6	3.1
In	≤43	≤54.0	Dy	3.3	2.9
Al	4	21.4	Gd	2.5	2.3
Cd	<10	<12.8	Ce	1.8	1.9
Cs	<5	<5.4	Sm	1.6	1.5
F	<0.5	<3.8	Ge	<0.5	<1.0

Table S2. Magnetic moments of Nd in different layers.

Calculations show that the surface magnetic moment is restored to the bulk value after three layers. The 4f contribution to the magnetic moment is 2.454 µB, the rest is induced in the 6s and 5d shells.

Layer	Magnetic moment (μ_B)	
	hexagonal surface termination	cubic surface termination
1st	2.89	2.91
2nd	2.79	2.81
Bulk cubic sites	2.66	
Bulk hexagonal sites	2.67	

References
1. S. F. Edwards, P. W. Anderson, Theory of spin glasses. *J Phys F: Met Phys* **5**, 965 (1975).
2. S. F. Edwards, P. W. Anderson, Theory of spin glasses. II. *J Phys F: Met Phys* **6**, 1927 (1976).
3. K. Binder, A. P. Young, Spin glasses: Experimental facts, theoretical concepts, and open questions. *Rev Mod Phys* **58**, 801 (1986).
4. M. Mezard, G. Parisi, M. A. Virasoro, *Spin Glass Theory and Beyond.* (World Scientific, Singapore, 1987).
5. K. H. Fischer, J. A. Hertz, *Spin Glasses.* (Cambridge University Press, 1993).
6. N. Katayama *et al.*, Investigation of the Spin-Glass Regime between the Antiferromagnetic and Superconducting Phases in Fe1+ySexTe1-x. *J Phys Soc Jap* **79**, 113702 (2010).
7. J. Hertz, A. Krough, R. G. Palmer, *Introduction to the theory of neural computation.* (CRC Press, 1991).
8. Y. Zhou, K. Kanoda, T.-K. Ng, Quantum spin liquid states. *Rev Mod Phys* **89**, 025003 (2017).
9. S. T. Bramwell, M. J. P. Gingras, Spin Ice State in Frustrated Magnetic Pyrochlore Materials. *Science* **294**, 1495 (2001).
10. B. Skubic *et al.*, Atomistic spin dynamics of the Cu-Mn spin-glass alloy. *Phys Rev B* **79**, 024411 (2009).
11. R. Rammal, G. Toulouse, M. A. Virasoro, Ultrametricity for physicists. *Rev Mod Phys* **58**, 765 (1986).
12. M. Mézard, G. Parisi, A tentative replica study of the glass transition. *J Phys A: Mat Theor* **29**, 6515-6524 (1996).
13. J. Schmalian, P. G. Wolynes, Stripe Glasses: Self-Generated Randomness in a Uniformly Frustrated System. *Phys Rev Lett* **85**, 836 (2000).
14. H. Westfahl, J. Schmalian, P. G. Wolynes, Self-generated randomness, defect wandering, and viscous flow in stripe glasses. *Phys Rev B* **64**, 174203 (2001).
15. A. Principi, M. I. Katsnelson, Self-Induced Glassiness and Pattern Formation in Spin Systems Subject to Long-Range Interactions. *Phys Rev Lett* **117**, 137201 (2016).
16. A. Principi, M. I. Katsnelson, Stripe glasses in ferromagnetic thin films. *Phys Rev B* **93**, 054410 (2016).
17. A. Kolmus, M. I. Katsnelson, A. A. Khajetoorians, H. J. Kappen, Atom-by-atom construction of attractors in a tunable finite size spin array. *New J Phys* **22**, 023038 (2020).
18. R. M. Moon, W. C. Koehler, W. Cable, Magnetic Structure of Neodymium. *J Appl Phys* **35**, 1041 (1964).
19. P. Bak, B. Lebech, Triple-Q-Modulated Magnetic-Structure and Critical Behavior of Neodymium. *Phys Rev Lett* **40**, 800 (1978).
20. B. Lebech, J. Alsnielsen, K. A. Mcewen, X-Ray and Neutron-Scattering Study of the Magnetic-Structure of Neodymium Metal. *Phys Rev Lett* **43**, 65 (1979).
21. E. M. Forgan, E. P. Gibbons, K. A. Mcewen, D. Fort, Observation of a Quadruple-Q Magnetic-Structure in Neodymium. *Phys Rev Lett* **62**, 470 (1989).
22. K. A. McEwen, S. W. Zochowski, Magnetic Phase-Transitions in Neodymium. *J Magn Magn Mater* **90-1**, 94 (1990).
23. S. W. Zochowski, K. A. Mcewen, E. Fawcett, Magnetic Phase-Diagrams of Neodymium. *J Phys. Condens. Matter* **3**, 8079 (1991).
24. E. M. Forgan *et al.*, Field Effects on the Antiferromagnetic Ordering of Neodymium. *J Magn Magn Mater* **104**, 911 (1992).
25. B. Lebech, J. Wolny, R. M. Moon, Magnetic Phase-Transitions in Double Hexagonal Close-Packed Neodymium Metal Commensurate in 2 Dimensions. *J Phys. Condens. Matter* **6**, 5201 (1994).
26. P. A. Lindgard, T. Chatterji, K. Prokes, V. Sikolenko, J. U. Hoffmann, Magnetic diffuse scattering from Nd above T-N and deduced exchange interaction parameters. *J Phys. Condens. Matter* **19**, 286201 (2007).
27. D. Wegner, A. Bauer, A. Rehbein, G. Kaindl, Exchange Splittings of Lanthanide (0001)-Surface States and Their Dependences on Short-Range Magnetic Order. *Jap J Appl Phys* **45**, 1941 (2006).
28. S. Heinze *et al.*, Spontaneous atomic-scale magnetic skyrmion lattice in two dimensions. *Nat Phys* **7**, 713 (2011).

29. D. Weller, S. F. Alvarado, Preparation of Remanently Ferromagnetic Gd(0001). *J Appl Phys* **59**, 2908 (1986).
30. S. C. Wu *et al.*, Surface-State on Clean Tb(0001). *Phys Rev B* **44**, 13720 (1991).
31. G. H. Fecher *et al.*, Dichroism in angular resolved VUV-photoemission from the (0001) surfaces of thin Gd and Nd films epitaxially grown on W(110). *Eur Phys J B* **11**, 161 (1999).
32. E. Weschke, G. Kaindl, 4f- and surface-electronic structure of lanthanide metals. *J Electron Spectros Relat Phenomena* **75**, 233 (1995).
33. K. M. Dobrich *et al.*, Fermi-Surface Topology and Helical Antiferromagnetism in Heavy Lanthanide Metals. *Phys Rev Lett* **104**, 246401 (2010).
34. C. Dufour *et al.*, Epitaxial growth of dhcp samarium: single crystal films and Sm/Nd superlattices. *J Cryst Growth* **234**, 447 (2002).
35. O. Waller *et al.*, Lattice dynamics of neodymium: Influence of 4 f electron correlations. *Phys Rev B* **94**, 014303 (2016).
36. E. Weschke, G. Kaindl, Magnetic exchange splitting in lanthanide metals. *J Phys. Condens. Matter* **13**, 11133 (2001).
37. J. Quinn, Y. S. Li, F. Jona, D. Fort, Atomic-Structure of a Gd(0001) Surface. *Phys Rev B* **46**, 9694 (1992).
38. J. P. Goff, C. Bryn-Jacobsen, D. F. McMorrow, R. C. C. Ward, M. R. Wells, Formation of uniform magnetic structures and epitaxial hydride phases in Nd/Pr superlattices. *Phys Rev B* **55**, 12537 (1997).
39. E. D. Tober, R. X. Ynzunza, C. Westphal, C. S. Fadley, Relationship between morphology and magnetic behavior for Gd thin films on W(110). *Phys Rev B* **53**, 5444 (1996).
40. S. Jo, Y. Gotoh, Growth modes of Nd deposited on Mo(110) surface. *Jap J Appl Phys* **38**, 6878 (1999).
41. H. Li *et al.*, Structural and Electronic-Properties of Ultrathin Films of Gd, Tb, Dy, Ho, and Er. *Phys Rev B* **45**, 3853 (1992).
42. M. Farle, K. Baberschke, U. Stetter, A. Aspelmeier, F. Gerhardter, Thickness-Dependent Curie-Temperature of Gd(0001)/W(110) and Its Dependence on the Growth-Conditions. *Phys Rev B* **47**, 11571 (1993).
43. C. S. Arnold, D. P. Pappas, Gd(0001): A semi-infinite three-dimensional heisenberg ferromagnet with ordinary surface transition. *Phys Rev Lett* **85**, 5202 (2000).
44. C. Schussler-Langeheine *et al.*, Magnetic splitting of valence states in ferromagnetic and antiferromagnetic lanthanide metals. *Phys Rev Lett* **84**, 5624 (2000).
45. E. Weschke *et al.*, Finite-size effect on magnetic ordering temperatures in long-period antiferromagnets: Holmium thin films. *Phys Rev Lett* **93**, 157204 (2004).
46. B. A. Everitt *et al.*, Helimagnetic structures in epitaxial Nd/Y superlattices and alloys. *Phys Rev B* **56**, 5452 (1997).
47. J. P. Goff *et al.*, Magnetism and superconductivity in neodymium/lanthanum superlattices. *Physica B* **241**, 714 (1998).
48. A. Aspelmeier, F. Gerhardter, K. Baberschke, Magnetism and Structure of Ultrathin Gd Films. *J Magn Magn Mater* **132**, 22 (1994).
49. M. Bode, M. Getzlaff, S. Heinze, R. Pascal, R. Wiesendanger, Magnetic exchange splitting of the Gd(0001) surface state studied by variable-temperature scanning tunneling spectroscopy. *Appl Phys A* **66**, S121 (1998).
50. S. s. materials, See supplementary materials. *See supplementary materials*.
51. S. Krause *et al.*, Consequences of line defects on the magnetic structure of high anisotropy films: Pinning centers on Dy/W(110). *Europhys Lett* **76**, 637 (2006).
52. M. Getzlaff, M. Bode, R. Pascal, R. Wiesendanger, Adsorbates on Gd(0001): A combined scanning tunneling microscopy and photoemission study. *Phys Rev B* **59**, 8195 (1999).
53. D. Wegner, A. Bauer, G. Kaindl, Effect of impurities on Tamm-like lanthanide-metal surface states. *Phys Rev B* **76**, 113410 (2007).
54. D. Wegner, A. Bauer, G. Kaindl, Magnon-broadening of exchange-split surface states on lanthanide metals. *Phys Rev B* **73**, 165415 (2006).
55. T. Hanaguri *et al.*, A 'checkerboard' electronic crystal state in lightly hole-doped Ca2-xNaxCuO2Cl2. *Nature* **430**, 1001 (2004).
56. S. Muhlbauer *et al.*, Skyrmion Lattice in a Chiral Magnet. *Science* **323**, 915 (2009).

57.   X. Z. Yu *et al.*, Real-space observation of a two-dimensional skyrmion crystal. *Nature* **465**, 901 (2010).

58.   K. von Bergmann, M. Menzel, A. Kubetzka, R. Wiesendanger, Influence of the Local Atom Configuration on a Hexagonal Skyrmion Lattice. *Nano Lett* **15**, 3280 (2015).

59.   W. C. Koehler, Magnetic Properties of Rare-Earth Metals and Alloys. *J Appl Phys* **36**, 1078 (1965).

60.   I. L. M. Locht *et al.*, Standard model of the rare earths analyzed from the Hubbard I approximation. *Phys Rev B* **94**, 085137 (2016).

61.   Y. O. Kvashnin *et al.*, Exchange parameters of strongly correlated materials: Extraction from spin-polarized density functional theory plus dynamical mean-field theory. *Phys Rev B* **91**, 125133 (2015).

62.   P. Loptien, L. Zhou, A. A. Khajetoorians, J. Wiebe, R. Wiesendanger, Superconductivity of lanthanum revisited: enhanced critical temperature in the clean limit. *J Phys. Condens. Matter* **26**, 425703 (2014).

63.   N. Romming *et al.*, Writing and Deleting Single Magnetic Skyrmions. *Science* **341**, 636 (2013).

64.   M. D. Ediger, Spatially Heterogeneous Dynamics in Supercooled Liquids. *Annu Rev Phys Chem* **51**, 99-128 (2000).

65.   T. L. Cocker, D. Peller, P. Yu, J. Repp, R. Huber, Tracking the ultrafast motion of a single molecule by femtosecond orbital imaging. *Nature* **539**, 263 (2016).

66.   H. Rieger, A. P. Young, in *Complex Behaviour of Glassy Systems,* M. Rubí, C. Pérez-Vicente, Eds. (Springer, Heidelberg, 1997).

67.   C. Chamon, Quantum glassiness in strongly correlated clean systems: An example of topological overprotection. *Phys Rev Lett* **94**, 040402 (2005).

68.   R. M. Nandkishore, M. Hermele, Fractons. *Annu Rev Condens Matter Phys* **10**, 295 (2019).

69.   H. von Allwörden *et al.*, Design and performance of an ultra-high vacuum scanning tunneling microscope operating at 30 mK and in a vector magnetic field. *Rev Sci Instr* **89**, 033902 (2018).

70.   J. M. Wills, Alouani, M., Andersson, P., Delin, A., Eriksson, O., Grechnyev, O. , *Full-Potential Electronic Structure Method.* (Springer, Heidelberg, 2010).

71.   https://github.com/UppASD/UppASD.

72.   O. Eriksson, A. Bergman, L. Bergqvist, J. Hellsvik, *Atomistic Spin Dynamics: Foundations and Applications.* (Oxford University Press, 2017).

73.   B. Kim, A. B. Andrews, J. L. Erskine, K. J. Kim, B. N. Harmon, Temperature-Dependent Conduction-Band Exchange Splitting in Ferromagnetic Hcp Gadolinium - Theoretical Predictions and Photoemission Experiments. *Phys Rev Lett* **68**, 1931 (1992).

74.   M. E. Davila, S. L. Molodtsov, C. Laubschat, M. C. Asensio, Structural determination of Yb single-crystal films grown on W(110) using photoelectron diffraction. *Phys Rev B* **66**, 035411 (2002).

75.   S. A. Nepijko *et al.*, Lattice relaxation of Gd on W(110). *Surf Sci* **466**, 89 (2000).

76.   H. Ott, C. Schussler-Langeheine, E. Schierle, E. Weschke, G. Kaindl, Depth-resolved magnetic structure across the ferromagnetic to helical-antiferromagnetic phase transition in Dy/W(110). *Phys Rev B* **82**, 214408 (2010).

77.   S. Soriano, C. Dufour, K. Dumesnil, A. Stunault, New magnetic phase and magnetic coherence in Nd/Sm(001) superlattices. *J Phys. Condens. Matter* **18**, 4995 (2006).

78.   E. D. Tober *et al.*, Observation of a ferromagnetic-to-paramagnetic phase transition on a ferromagnetic surface using spin-polarized photoelectron diffraction: Gd(0001). *Phys Rev Lett* **81**, 2360 (1998).

79.   A. Bauer, A. Muhlig, D. Wegner, G. Kaindl, Lifetime of surface states on (0001) surfaces of lanthanide metals. *Phys Rev B* **65**, 075421 (2002).

80.   L. Berbil-Bautista, S. Krause, M. Bode, R. Wiesendanger, Spin-polarized scanning tunneling microscopy and spectroscopy of ferromagnetic Dy(0001)/W(110) films. *Phys Rev B* **76**, 064411 (2007).

81.   M. Bode *et al.*, Temperature-dependent exchange splitting of a surface state on a local-moment magnet: Tb(0001). *Phys Rev Lett* **83**, 3017 (1999).

82.   M. Bode, M. Getzlaff, R. Wiesendanger, Spin-polarized vacuum tunneling into the exchange-split surface state of Gd(0001). *Phys Rev Lett* **81**, 4256 (1998).

83.   M. Bodenbach, A. Hohr, C. Laubschat, G. Kaindl, M. Methfessel, Surface Electronic-Structure of Tm(0001) and Yb(111). *Phys Rev B* **50**, 14446 (1994).

84. M. Donath, B. Gubanka, F. Passek, Temperature-dependent spin polarization of magnetic surface state at Gd(0001). *Phys Rev Lett* **77**, 5138 (1996).
85. B. A. Everitt *et al.*, Magnetic-Ordering of Nd in Nd/Y Superlattices. *J Magn Magn Mater* **140**, 769 (1995).
86. F. Heigl *et al.*, Annealing-induced extension of the antiferromagnetic phase in epitaxial terbium metal films. *Phys Rev B* **72**, 035417 (2005).
87. E. Lundgren *et al.*, Geometry of the valence transition induced surface reconstruction of Sm(0001). *Phys Rev Lett* **88**, 136102 (2002).
88. K. Maiti, M. C. Malagoli, A. Dallmeyer, C. Carbone, Finite temperature magnetism in Gd: Evidence against a Stoner behavior. *Phys Rev Lett* **88**, 167205 (2002).
89. A. Melnikov *et al.*, Picosecond magnetization dynamics of the Gd(0001) surface. *J Magn Magn Mater* **272**, 1001 (2004).
90. C. Ostertag *et al.*, Dichroism in VUV photoemission from the (0001)-surfaces of ultrathin Gd and Nd films on W(110). *Surf Sci* **377**, 427 (1997).
91. H. Realpe *et al.*, Islands as Nanometric Probes of Strain Distribution in Heterogeneous Surfaces. *Phys Rev Lett* **104**, 056102 (2010).
92. A. Rehbein, D. Wegner, G. Kaindl, A. Bauer, Temperature dependence of lifetimes of Gd(0001) surface states. *Phys Rev B* **67**, 033403 (2003).
93. E. Weschke *et al.*, Temperature dependence of the exchange splitting of the surface state on Gd(0001): Evidence against spin-mixing behavior. *Phys Rev Lett* **77**, 3415 (1996).
94. M. Bode, S. Krause, L. Berbil-Bautista, S. Heinze, R. Wiesendanger, On the preparation and electronic properties of clean W(110) surfaces. *Surf Sci* **601**, 3308 (2007).
95. P. Kurz, G. Bihlmayer, S. Blugel, Magnetism and electronic structure of hcp Gd and the Gd(0001) surface. *J Phys. Condens. Matter* **14**, 6353 (2002).
96. A. C. Jenkins *et al.*, The relationship between interlayer spacing and magnetic ordering in gadolinium. *J Phys. Condens. Matter* **12**, 10441 (2000).
97. W. Kohn, Density functional and density matrix method scaling linearly with the number of atoms. *Phys Rev Lett* **76**, 3168 (1996).
98. N. Metropolis, A. W. Rosenbluth, M. N. Rosenbluth, A. H. Teller, E. Teller, Equation of State Calculations by Fast Computing Machines. *J Chem Phys* **21**, 1087 (1953).
99. B. Skubic, J. Hellsvik, L. Nordström, O. Eriksson, A method for atomistic spin dynamics simulations: implementation and examples. *J Phys. Condens. Matter* **20**, 315203 (2008).
100. L. Lundgren, P. Svedlindh, P. Nordblad, O. Beckman, Dynamics of the Relaxation-Time Spectrum in a CuMn Spin-Glass. *Phys Rev Lett* **51**, 911 (1983).